Master Thesis

Holocene sediment budget and sediment dynamics of Lake Sils in the Upper Engadin

Florian Donau

Supervisor

Prof. Dr. Michael Strasser, Institute of Geology, ETH Zürich

Co-Supervisor

Dr. Florian Kober, Institute of Geology, ETH Zürich

Additional Supervisor

Reto Grischott, Institute of Geology, ETH Zürich

View from Piz da la Margna towards Lake Sils and Lake Silvaplana to the north. (Photo taken by Markus Loher during field campagin in September 2013)

Abstract

In an open source to sink model the denudation rate of a catchment area should be directly linked to the sedimentation rate in the sink. Lake Sils in the upper Engadin receives the majority of its sedimentary supply from the catchment area of the Val Fedoz and therefore represents such a sink. Published sediment-budget-based erosion rates for the last deglaciation periods suggest 12 to 14 fold higher rates compared to catchment wide denudation rates resulting from on ^{10}Be cosmogenic nuclide data and modern sediment yields in Alpine regions. This study tried to evaluate these observations by quantifying the sedimentation rates in a sink over the last deglaciation and Holocene period in the Upper Engadin.

High resolution single channel pinger seismic data was combined with two long piston cores from distal and proximal positions in relation to the major tributary inlet (Fedoz River with Isola Delta). Physical property measurements, X-ray fluorescence (XRF) scans, carbon content measurements with the coulometric method and thin section analyses of the sediment were combined with AMS radiocarbon dating to reconstruct the Holocene sedimentation history of the lake. In combination with the seismic survey, isopach maps and time series of sedimentation rate were generated.

The pattern of the sediment distribution confirms that the Fedoz River with the Isola Delta acted as a major tributary during the Holocene period. However, the seismic data indicates the existence of a second sediment tributary system during the Younger Dryas period on the Maloja side. A termination of this delivery system is indicated by the sudden change in the sediment geometry of the sediment units suggesting the Forno glacier as a source.

A comparison of the sediment yield into Lake Sils with alpine climate records shows a correlation with a south alpine climate trend during the Holocene Thermal Maximum. As mentioned in several other studies, the Holocene Thermal Maximum started ca 4000-5000 years earlier in the Southern Alps compared to the Northern Alps. The obtained results reveal that Lake Sils has responded in a similar way.

Even though the distal core location shows the general sedimentological trend of Lake Sils, comparison of the sedimentation rates to a paraglacial cycle only indicates a minor correlation. The sedimentation rate in the proglacial sediments is roughly estimated and varves in the Younger Dryas period show slightly increasing thicknesses of around 2.0mm to 2.2mm per year in an upward direction. Judging from this data the regional climate must have had a larger influence on the sedimentation rate than the general proglacial sediment yield cycle in the Holocene.

Zusammenfassung

In einem Source to Sink Model sollten die Sedimentationsraten der Senke direkt vergleichbar sein mit der Abtragung im Einzugsgebiet. Der grösste Teil des Sedimenteintrags in den Silsersees im Ober Engadin, als Senke eines solchen Systems, stammt aus dem Val Fedoz. Publizierte Erosionsraten basierend auf Sedimenationsraten für das Ende der letzten Eiszeit deuten auf 12 bis 14 fach höhere raten im Gegensatz zu Erosionsraten des gesamten Einzugsgebietes basierend auf ^{10}Be kosmogenen Nukliden und heutigen sediment transport Raten. Diese Studie versucht diese Erkenntnisse zu überprüfen und die Errosionsraten seit der letzten Eiszeit und im Holozän zu quantifizieren.

Eine hochauflösende Einkanal-Pinger-Seismik Kampagne kombiniert mit zwei langen sediment Kernen an proximaler und distaler Position in Bezug auf den Fedoz Bach mit dem Isola Delta als Hauptzufluss. Physikalische Eigenschaften, Element Konzentrationen mit Röntgen Fluoreszenz sowie der Kohlenstoff Gehalt mit den Coulometrischen Verfahren wurden gemessen, Sediment Dünnschliffe wurden analysiert. Kombiniert mit AMS Radiokarbon Datierungen wurde die Holozäne sediment Geschichte des Sees rekonstruiert. Isopachen Karten und Zeitreihen der Sedimentationsraten wurden erstellt.

Die Sedimenteinfühlung bestätigt den Fedoz Bach als den Haubtzufluss während des ganzen Holozäns. Zusätzlich deuten die seismischen Daten auf einen zweiten Hauptzufluss von der Maloja Seite an, welcher mindestens bis zur Jüngeren Dryas Zeit aktiv war. Das plötzliche Ende dieses Zuflusses lässt auf den Forno Gletscher als Quelle schliessen.

Ein Vergleich der Sedimentationsraten im Silsersee mit Klimaaufzeichnungen in den Alpen zeigen eine Korrelation mit den Südalpinen Klima Änderungen. Wie aus andern Studien bekannt ist, beginnt das Holozäne Thermale Maximum in den Südalpen 4000-5000 Jahre früher als in den Nordalpen. Diese Studie zeigt, dass der Silsersee ebenfalls diesem Klima Trend folgt.

Des weiteren zeigt der distale Kern Sils13_1 den generellen sedimentologischen Trend im See. Eine teilweise Übereinstimmung mit dem Paraglazialen Zyklus Model konnte gefunden werden. Jedoch sind die Sedimentationsraten in der frühen Zeit des Gletscherückgans nicht genau bekannt sowie zeigen Warven während der Jüngeren Dryas einen anstieg der Sedmentationsrate im Bereich von 2.0mm bis 2.2mm pro Jahr. Aus diesen Daten geht hervor, dass das regionale Klima einen weit höheren Einfluss auf die Sedimentationsraten im Silsersee hatten als der paraglaziale Zyklus während der Holozänen Zeit Periode.

Contents

List of Tables

List of Figures

1 Introduction

Denudation rates of a catchment area and the sedimentation rates in an adjacent basin should be comparable with respect to the clastic components. Nonetheless, transport of fine particles and elements in solution need to be accounted for as well (Einsele & Hinderer, 1998). Under the assumption of a closed source to sink model where no sediment storage occurs and sediment transport happens immediately, it can be expected that the denudation rate in the source area is equal to the sedimentation rate in the sink (Bierman & Steig, 1996). Catchment wide denudation rates based on cosmogenic nuclides and basin infilling rates obtained since the last glacial maximum suggest 12 to 14 fold higher alpine denudation rates compared to modern estimates (Hinderer, 2001).

In the ongoing PhD thesis of Reto Grischott a time series of denudation rates based on ^{10}Be cosmogenic nuclides is set up to try to understand the driving forces of denudation rate changes and their correlation to climate changes in the Alps and the Bolivian Andes. Changes in denudation rates in the source area and the sediment supply to the sink over the same time period can be verified in lake sediments in a nearly closed system. Lake Sils and its catchment is a study object in the PhD thesis of Reto Grischott. This study analyzed Lake Sils as the sink part of the system and produced time series of sedimentation rates and examined the sediment distribution in the Maloja Basin. The sedimentation rates are set contrast with the regional climatic and geomorphic context.

1.1 Study area

Lake Sils is the upper and southernmost lake of the four Upper Engadin lakes and lies between Sils and the Malojapass (see Figure 1). The 1797 m.a.s.l. high lake has a major part of its catchment area in the Val Fedoz to the south-east. The Aua da Fedoz acts as major tributary which builds up the Isola Delta on the south-east side of the lake. The north-eastern neighboring valley of the Val Fedoz is the Val Fex which is of comparable size and currently drains towards Lake Silvaplana. The Inn river drains the Engadin towards north-east. The Bergell valley is situated south of the Malojapass with its north-easternmost side valley Val Forno. The region around Sils and the upper Engadin is a well studied region in the Alps. Generations of geologists have studied and mapped the area, its pre-alpine history and its formation since the last ice age to the Holocene climate variations (Hantke, 1983; Maisch, 1992; Spillmann, 1993; Ohlendorf, 1999; Spillmann & Tromsdorff, 2005; Blass et al., 2005).
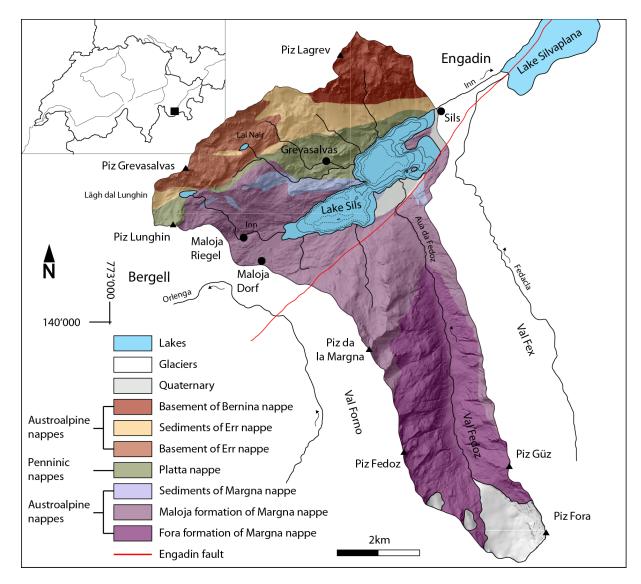
Figure 1: Geological map of the catchment area of Lake Sils modified after Spillmann (1993) and based on data from swisstopo (2014a) and swisstopo (2014c).

1.1.1   Tectonic units and nappes

The Penninic nappes and the overlying Austroalpine nappes are the major tectonic units of the catchment area of Lake Sils (see Figure 1). The southern and eastern parts of the catchment area lie within the Margna nappe. This lowermost Austroalpine unit can be divided into a Maloja formation located in the upper and a Fora formation in the lower Fedoz valley. The Mesozoic sediment cover of the Margna nappe outcrops on the north-east shore of the Maloja basin (see Figure 1). The crystalline rocks of the Austroalpine nappes are composed of chlorite-mica-gneisses. Mafic layers and carbonates are found interbedded with the crystalline rocks (Spillmann & Tromsdorff, 2005). The Fedoz metamorphic Gabbro is found near the Fedoz glacier as well as in lenses between the Fora and Maloja formation and it is composed of chlorite-

actinolite-epidote-schists and gneisses (Spillmann & Tromsdorff, 2005).

To the north of Lake Sils, the mid Austroalpine Bernina and Err nappes are outcropping. They are composed of granites, diorites of the Piz Grevasalvas and the Piz Lagrev and a sedimentary cover consisting of dolomites and schists of Triassic and Jurassic age (Cornelius, 1935). A wedge of the Penninic Ophiolites from the Platta nappe is found on the western side of the lake. This ultramafic nappe is the only source of serpentinite grains brought into the lake (Cornelius, 1951; Ohlendorf, 1999). South of the Margna nappe are the Malenco unit and the Bergell intrusion outside of the catchment exposed.

The geological units around the lake are displaced by the Engadin fault. Kinematics studies are revealed an oblique slip and block rotation, with an uplift in the south-eastern block in the Maloja region, no vertical movement in the Samedan area and a strike-slip component with downfaulting in the northern most part around S-chanf (Schmid & Froitzheim, 1993). The dextral strike slip displacement was estimated to three to six kilometers (Trümpy, 1977). The Engadine fault is considered to be active in Pleistocene age and the latest main deformation in the Maloja Pass area mostly took place in the interval 15.7k to 2.5k cal. years BP (Tibaldi & Pasquare, 2008). In some literature this fault is also referred to as the Engadin Line (Trümpy, 1977; Spillmann & Tromsdorff, 2005).

1.1.2 Quaternary

The lake basin itself was created by glacial over-deepening during the last glacial periods (Hantke, 1983). The local glaciers filled the valley to a height of 2800 m.a.s.l. during the Last Glacial Maximum (Florineth & Schlüchter, 2000; Suter, 1981). The Engadin main valley was free of ice at the end of the Samedan stage in the late Wurm, comparable with the Daun stage at around 13k years BP uncalibrated (Maisch et al., 2003)(see Figure 2). The glaciers from the Val Fex and Val Fedoz reached into the newly formed lakes (Hantke, 1983; Burga, 1997).

After the glacier retreat Lake Champfer, Lake Silvaplana and Lake Sils were connected based on drill data at Sils Maria site (Elsasser & Boesch, 1991). The cuttings of this drill core revealed lake and delta sediments overlying a basal moraine of unknown age at a depth of 48m to 113m below surface (Elsasser & Boesch, 1991). In 1973 9% of the total catchment of Lake Sils was glaciated (Maisch, 1992) in 1992 it was 8% (Blass et al., 2005). A glacial cover of 5% was excluded of the latest data from swisstopo (2014b).

1.1.3   Holocene

The Val Fedoz is a hanging valley with a trough shoulder above the Isola Delta. The lower part of the shoulder is forested, the main valley floor is covered with meadows. Side walls are mostly characterized by bedrock exposure or are covered with colluvial deposits or bedrock (see Figure 2). In the Egesen stage from 11k years BP uncalibrated the glaciers terminated behind the outlet of the Val Fedoz (Maisch, 1992). Climate variations in the Holocene lead to three glacier retreat phases in the Tschierva glacier area, 10km east of Lake Sils, around 9.2k cal. years PB, from 7.45k to 6.65k cal. years PB and from 6.2k to 5.6k cal. years PB (Joerin et al., 2008). A cold period with glacier advantage in the time of 8.6k to 8k cal. years PB was referred to as the Kromer stage in the Austrian alps (Kerschner et al., 2006). The next glacial high stand was in the Little Ice Age at about 1850 (Maisch, 1992). In 2009 the glacier covered 14.9% of the Val Fedoz swisstopo (2014a). After glacier retreat some rockfall deposits and colluvial fans were formed, although rock glaciers are still active on the western valley side (Vogel, 1995).
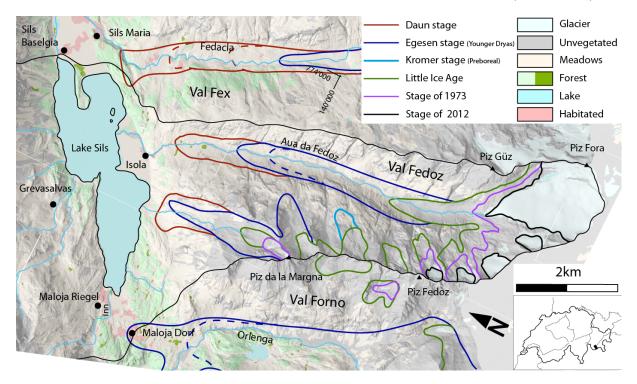
Figure 2: Topographic map with surface cover and glacier stages after swisstopo (2014b,c); Maisch (1992).

1.1.4   Lake Sils Bathymetry

Lake Sils can be subdivided into four sub-basins (see Figure 3). The Central Basin is the largest and deepest with a depth of about 71m. The Lagrev Basin to the north and the Sils Basin to the

north-east are two smaller side basins of the Central Basin with water depths of around 30m. The Maloja Basin to the south is about 30m to 35m deep and is divided into two sub-basins by a small ridge striking east-west. The Maloja Basin is separated of the Central Basin by the Isola Delta and its bedrock peninsula the Piz d'Islas (See Figure 3).

1.1.5 Limnology

Lake Sils has a volume of $137 * 10^6 m^3$, a surface area of $4.1 km^2$, a residence time of 2 years and a catchment area of $45.7 km^6$ (LIMNEX, 1994). The oligotrophic lake shows a dimictic behavior with a short mixing phase in spring after ice break up, a summer stratification with a thermocline in 20m to 30m depth and a second mixing period in November (Bosli-Pavoni, 1971). With the relatively low phosphate-phosphorus content of $5\mu g/l$ and a total phosphorus content of $11\mu g/l$ Lake Sils is able to hold 0.06 to 1.85mg/l of biomass (Bosli-Pavoni, 1971). With a low biologic production and high classic input the lake sediments are dominated by the clastic components (Ohlendorf, 1999).

1.1.6 Climate

Climate data for the Upper Engadin region are obtained by the Federal Office of Meteorology and Climatology MeteoSwiss at Sils Maria next to lake Sils. An anual mean temperature of 2.3°C with monthly amplitude of 18.3°C and a mean annual precipitation of 1011mm water in the time from 1981 to 2010 are characteristics of the cold continental climate in the high alpine valley (Federal Office of Meteorology and Climatology MeteoSwiss, 2014). The precipitation with 1200mm per month is twice as much in summer as in winter with 500mm per month and follows the temperature curve (Federal Office of Meteorology and Climatology MeteoSwiss, 2014). A small cloud cover enables above average summer temperatures and temperature inversion leads to cold winters in comparison of the Upper Engadin to other alpine regions (Gensler, 1978). The typically north-westward wind regime has a small effect on the Upper Engadin, the water carrying air masses come mostly over the Malojapass (Gensler, 1978).

The strong valley wind, locally called 'Malojawind' is a peculiarity of the Upper Engadin. This wind occurs during sunny summer days when a local low pressure cell develops in the Engadin which sucks up air from the Bergell valley over the Maloja pass (Gensler, 1978).
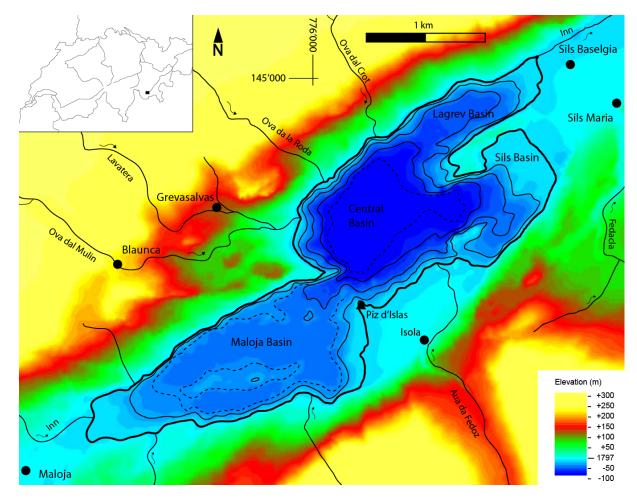
Figure 3: Bathymetry map of Lake Sils with surrounding topography based on seismic survey of this study and (Blass et al., 2005) and data of swisstopo (2014a).

1.2   Previous limnogeological studies on Lake Sils

Lake Sils was investigated by Leemann & Niessen (1994), but the cores were not described in that PhD thesis (Leemann & Niessen, 1994). In 1994 C. Ohlendorf did a PhD thesis on the four Engadin lakes where analog single channel pinger seismics, five short cores, three long piston cores and water property profiles were taken from Lake Sils. The minerals of the most recent sediments of the eight cores and all main tributaries were analyzed with X-ray diffraction (XRD) for their mineral composition (Ohlendorf, 1999). After discovering that Lake Sils is not varved like Lake Silvaplana the study on Lake Sils was not further pursued.

22 short cores were taken from Lake Sils and a 14km long high resolution seismic survey with a 3.5kHz single channel pinger system was recorded by Blass et al. (2005). Two remaining cores from Ohlendorf (1999) were opened and described in that study as well. In comparison to the

Central Basin where penetration is limited to 4m the seismic data in the Maloja Basin shows a deeper penetration up to 20m. The reduced penetration in the Central Basin was explained by trapped gas in the large mass flow event (Blass et al., 2005). This mass movement was dated with two samples to 600AD and 700AD (Blass et al., 2005). Due to sediment remobilization the younger age is used as maximum age. It was interpreted as a delta collapse from the Isola Delta into the Central Basin (Blass et al., 2005). Wohlwend (2010) found evidence, that the MF1 event created a tsunami with back flow currents at the Sils Maria site (See Figure 2). Furthermore, a present day sedimentation rate of about 1.1mm to 0.7mm per year was measured by Blass et al. (2005) with sediment traps.

2 Goal

2.1 Scientific question

The aim of this study is the create a time series of the sediment infilling in Lake Sils to construct a record of the sink in the source to sink model applied in the PhD thesis of Reto Grischott. This study analyzes the sediment filling of the Maloja Basin and answer different questions.

- Gives the seismics information about the sediment distribution in the Maloja Basin.

- Are there more Mass Transport Events in the Lake comparable with the Event described in Blass et al. (2005).

- Can a time series of sedimentation rates be produced, representative for the whole Lake Sils catchment and the Fedoz catchment.

- Are their changes in sedimentation rate and are they correctable to Lake Silvaplana and to climate records in the Alps.

- Can driving forces be evaluated and their influence quantificated.

- Is it possible to adapt the model of the sediment yield in a paraglacial cycle after Church & Ryder (1972) to the sedimentation rates in Lake Sils.

3   Materials and methods

3.1   Field campaign

3.1.1   Seismic acquisition

During the first week of September 2013 high resolution seismics was acquired with a Geoacoustic 3.5kHz single channel pinger system. The pinger was fixed approximately 40cm below the water surface on an inflatable catamaran which was pushed in front of a motor boat. The positioning was done with a Garmin GPSmap76Cx hand GPS system coupled with the Fugawi navigation software. The Octopus Marine 760 Shallow Seismic Processor recorded the seismic signal together with the GPS signal in the SEG-Y format. The pinger signal was triggered every 400ms. A sampling rate of 24390Hz and a recording time of 400ms lead to a sample interval of $41\mu s$ with 9756 samples per trace and a Nyquist frequency of 12195Hz. With a boat velocity of 5km/h to 7km/h a trace spacing of around 50cm to 70cm was achieved. The vertical resolution is given by equation $\lambda/4$ (Chopra et al., 2006). With a constant seismic velocity of 1450 m/s and wavelength of 41cm a vertical resolution of 10cm was resolved. A dense grid of lines was obtained in the Maloja Basin and around the Isola Delta (Figure 4). Details to the seismic processing are found in Section 3.4.1.

3.1.2   Coring campaign

Two piston cores were taken from an UWITEC platform (Niederreiter, 2013). Core Sils13_1 was taken in the Maloja Basin at 32 meter water depth and reaches a sediment depth of 13m. The core Sils13_2 is located about 150m from the Isola Delta in a small distal plateau in about 14.5 meter below water level and reaches a depth of 10.5 meter sediment (see Figure 4).

A 3 meter long and 63mm wide PVC liner was locked in a steel tube with the piston at the front and a percussion bar at the top. This setting was then hammered into the sediment. At the target depth of coring the piston was released and stayed at the fixed depth while the liner was pushed 3 meter into the sediment. Every 3 meters long liner was taken with a vertical overlap of 0.5 meter to the above and below liner section. Each 3 meter long liner was cut into approximately 1 meter long pieces. Additionally on both sites gravity short cores were taken with a length of about 1 meter. The cores are stored in the cold storage room at ETH Zurich at a temperature of 4°C. The sections are named after the lake, the year, the core location, 3m liner and cut section from top to bottom.
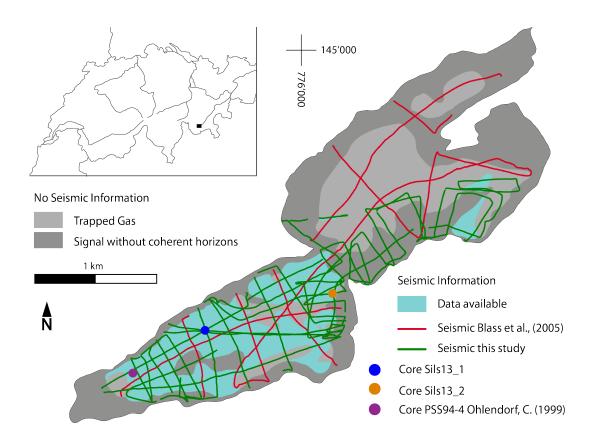
Figure 4: Map of core Sils13_1 and Sils13_2 of this study, core PSS94-4 of Ohlendorf (1999) and seismic lines with observed penetration on lines and interpolated over the Maloja Basin. Seismic data of this study and Blass et al. (2005).

3.2   Sediment analysis

3.2.1   MSCL

Gamma attenuation bulk density, the magnetic susceptibility and the p-wave velocity of the full cores were measured with the GEOTEK multi-sensor core logger of ETH Zurich in 5mm step size and a measuring interval of 10s (Geotek Limited, 2013).

3.2.2   Core splitting, scanning, and description

The core liners are cut on two sides with a rotating drill pit, two copper plates are then stuck through the cores. The copper plates are carefully pulled off sidewards of the cores after splitting. A line scan was taken right after opening, a second scan after 4 to 5 hours oxidization. The camera has a resolution of 363 dpi on the core surface. A white and black balance calibration was applied for all scans.

An initially visual core description was made and the liner sections were correlated. The photos and MSCL measurements where cut and merged to the composite core for each core (see Table 1). The section changes were made on characteristic horizons which are found on both overlapping

Table 1: Composition of core sections for composite core Sils13_1.

Section	section from mm	composite from mm	section to mm	to composite to mm	section change at
Sils13_1_7_sc	45	0	935	890	base of bright claycap
Sils13_1_1_a	700	890	862	1052	
Sils13_1_1_b	18	1052	656	1690	base of dark layer
Sils13_1_2_b	672	1690	1010	2028	
Sils13_1_2_c	10	2028	844	2862	base of dark layer
Sils13_1_3_a	212	2862	925	3575	
Sils13_1_3_b	2	3575	1017	4590	
Sils13_1_3_c	2	4590	784	5372	base of stronger bright layer
Sils13_1_4_a	278	5372	906	6000	
Sils13_1_4_b	124	6000	1009	6885	
Sils13_1_4_c	77	6885	962	7770	fine reddish layer
Sils13_1_5_a	418	7770	871	8223	
Sils13_1_5_b	1	8223	650	8872	
Sils13_1_5_c	5	8872	1255	10122	fluidized layer center
Sils13_1_6_a	193	10122	922	10851	
Sils13_1_6_b	3	10851	1016	11864	
Sils13_1_6_c	4	11864	1015	12875	
Sils13_1_2_a					not part of composite core

horizons.

Table 2: Composition of core sections for composite core Sils13_2.

Section	section from mm	composite from mm	section to mm	to composite to mm	section change at
Sils13_2_1_sc	45	0	1063	1018	fine dark layer
Sils13_2_2_b	306	1018	927	1639	
Sils13_2_2_c	98	1639	852	2393	top of coarser layer
Sils13_2_3_a	423	2393	635	2605	
Sils13_2_3_b	107	2605	990	3488	
Sils13_2_3_c	48	3488	622	4062	base of dark layer
Sils13_2_4_a	102	4062	709	4669	
Sils13_2_4_b	132	4669	981	5518	
Sils13_2_4_c	122	5518	908	6304	fine brighter layer
Sils13_2_5_a	146	6304	627	6785	
Sils13_2_5_b	77	6785	713	7421	
Sils13_2_5_c	119	7421	974	8276	
Sils13_2_6_a					not part of composite core
Sils13_2_6_b					not part of composite core
Sils13_2_6_c					not part of composite core
Sils13_2_2_a					not part of composite core

3.2.3 Smear slides

For the analysis of the sediment components smear slides were made. A small amount of sediment was dispersed on a glass plate and sealed with Nordland Optical Adhesive 61 glue and hardened under UV light. A refractive index of 1.56 enabled the analysis with a polarized light optical microscope. The identification was done with the database of westerndiatoms.colorado.edu.

3.2.4 Thin sections

Seven thin sections were made to characterize laminations and sediment structures. The sediment was taken with 1.5cm times 3cm wide plastic boxes. The samples were shock frozen with liquid nitrogen to avoid ice crystal formation and dried in a freeze dryer for three days. A 40% to 60% mixture of Laromin C 260 and Araldit DY 026 SP was put over the dry samples and

hardened over night at 60°C. The hard samples were then fixed on glass plates and polished down to $30\mu m$ thickness. Observations were done with a polarized light optical microscope.

3.2.5 Carbon content by the Coulometric method

The inorganic carbon and the total carbon content of 61 samples was measured with the CM5012 CO_2 coulometer from UIC Coulometrics at ETH Zurich. Roughly 50mg to 100mg of sediment were taken with a spatula and dried in a freeze dryer for about three days. 10mg of homogenized material was measured with the coulometer. The inorganic carbon was dissolved to CO_2 with HCl. The sample was burned at 950°C with pure oxygen for the total carbon. The produced amount of CO_2 is then measured with the coulometric titration method. Pure $CaCO_3$ was used as standard. For further information about the method see Herrmann & Knake (1973).

3.2.6 XRF Scanning

Selected sections, characteristic of the specific lithotypes, were measured with the Avaatech XRF Core Scanner. To characterize the thin beds a step size of 1mm was applied to most of the measurements. Selected longer sections were measured in 5mm steps. A detailed description of the method is given in (Richter et al., 2006). Five-fold repetitive measurements were applied every fiftiest measurement to estimate the mean deviation of the measurements (Westerhold, 2003).

Table 3: Settings if Avaatech XRF Core Scanner

	Slit size		X-Ray tube			
Step size	down core	cross core	Voltage	Current	Count Time	Filter
5 mm	5 mm	12 mm	10 kV	500 mA	10 s	no filter
5 mm	5 mm	12 mm	30 kV	2000 mA	30 s	Pd thick
1 mm	1 mm	12 mm	10 kV	1500 mA	20 s	no filter
1 mm	1 mm	12 mm	30 kV	2000 mA	40 s	Pd thick

The matrix effect and the grain size have an influence on the measurements. The density and organic substances also have an effect on all elements (Marguí et al., 2009). The water content and the formation of a water layer below the cover foil during the measurements influence the different elements in different manner (Tjallingii et al., 2007). While Al and Si counts are lowered in wet conditions Cl counts are increased, while K, Ca, Ti and Fe show no strong variations (Tjallingii et al., 2007). Additionally the organic matter has a high influence on the

XRF core scanning results (Löwemark et al., 2011). Due to the different influence of grain size density, water content and matrix effects of each mineral within the core, the counts of two different elements cannot be compared in a straight forward way. A comparison of count ratios instead of counts eliminates and minimizes grain size and matrix effects and thus enables element comparisons in different sediment types. The individual behavior of different elements has to be accounted for as well.

The element counts in the XRF core scans are influenced by the density in a linear way. The higher the density the more material and subsequently more elements are within the measurable area (Röhl & Abrams, 2000). A common Si source of lacustrine sediment is quartz, while Al is concentrated in clay minerals. Quartz grains are more robust to crushing than clay minerals and micas during transport therefore the Al/Si ratio is a relative grain size proxy (Cuven et al., 2010). As the Fe/Ti ratio is nearly constant it can be assumed that Fe is not influenced by the oxygen activity (Naeher et al., 2013) . With Mn being more sensitive to reducing conditions than Fe, the Mn/Fe ratio can be used as a relative redox proxy in the sediment core (Naeher et al., 2013).

3.3   AMS radiocarbon dating

Ten macro fossil samples were measured at the AMS laboratory of Ion Beam Physics at Hönggerberg, ETH Zurich, in collaboration with Irka Hajdas. Samples C14_1 and C14_4 are directly taken out of the cores. The other samples are washed trough a $125\mu m$ sieve and then picked under the binocular microscope. The samples were then measured in the lab at Hönggerberg. The results were calibrated with Oxcal 4.2.3 (Bronk Ramsey, 2013) on the IntCal13 atmospheric curve (Reimer et al., 2013)(Details to the samples and results are listed in Table 5 on Page 38).

3.4   Seismic data analysis

3.4.1   Seismic Processing

The SEG-Y coordinates were transformed into the Swiss LV03 coordinate system. The coordinates of the GPS were measured every 2 seconds and were interpolated in between the seismic traces.

The seismic data was then processed with SeisSpace ProMAX, the settings of the applied filters are listed in Table 4. First a DC removal filter was applied to remove the constant shift of the signal. A characteristic noise with a constant frequency over the whole 2 day survey was detected. A spectral analysis of the data shows the distinct noise frequencies (see Figure 5).

These frequency peaks where cut out with five Notch filters (Figure6). This noise is probably generated from the equipment itself. Finally a Bandpass filter was applied to the data.
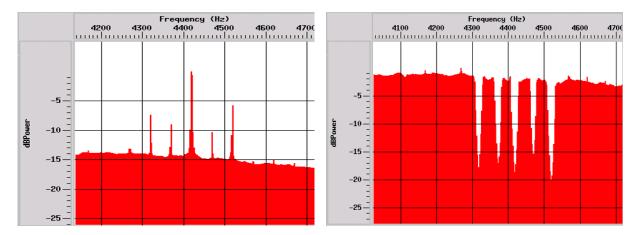
Figure 5: Spectral analysis of line 8 from trace 501 to 1000 after dc removal

Figure 6: Spectral analysis of line 8 from trace 501 to 1000 after application of all filters.

Table 4: Settings of ProMAX filters

Notch filters	Center (Hz)	Width (Hz)	Bandpass filter	(Hz)
	4318	20	from	1800
	4372	20		2500
	4472	20		6000
	4470	16	to	7000
	4520	22		

The straight and complete parts of the seismic lines were migrated with constant velocity of 1450m/s. On curved lines artifacts appeared during the migration. Additionally artifacts occurred on steeply dipping horizons (see Figures 7 and 8). These result from a too wide trace spacing for the given maximum frequency. Equation (1) gives maximum dip at a given frequency, velocity and trace spacing. This so called aliasing effect could have been avoided in most cases with a trace spacing of the order of 20cm with respect to the applied 3.5kHz pinger system and a maximum frequency of 6kHz in the Bandpass filter (Yilmaz, 2001).

Equation of maximum dip for Migration after (Yilmaz, 2001) (1)

dx = trace spacing
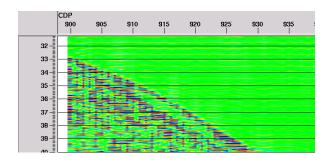
θ = dip angle

v = medium velocity

$$F_{max} = \frac{v}{2dx\sin\theta}$$

F_{max} = maximum frequency

16
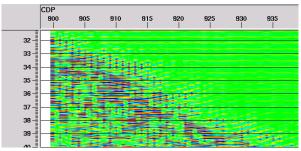
Figure 7: Line 8 from trace 900 to 940 with the processed data, Trace Display with smoothed color raster in Promax

Figure 8: Line 8 from trace 900 to 940 with the migrated data, Trace Display with smoothed color raster in Promax

Due to these aliasing problems migration was not applied and the analysis was performed on the nonmigrated data.

3.4.2 Data evaluation with IHS Kingdom Suite

The seismic data were interpreted with the IHS Kingdom Suite software. Seismic units were distinguished and correlated over the available data of the survey (see Figure 4)

Trapped gas as product of microbiological activity in the sediment limits the penetration of high resolution pinger seismic (Johnson et al., 1987; Blass et al., 2005)(an example is shown and described in Section 4.2.2 with Figure 29). Coarser material such as sand and gravel is brought in with the river on the delta slope or with colluvial processes near the shore line. This material absorbs much of the seismic energy and produces overlapping hyperbolas, which hinders the extraction of information (Adams et al., 2001). Additionally organic matter from the river inflow may increase the production of methane gas as a further drawback to the seismic data quality (Johnson et al., 1987; Adams et al., 2001).

3.4.3 Sediment-seismic correlation

The correlation with core Sils13_1 was based on the density measurements of the MSCL and the sediment characteristics. A high amplitude reflection is produced by high impedance contrasts between different sediment layers, where impedance is the product of the density and the wave velocity (Oldenburg et al., 1983). Since the velocity is assumed to be constant the density directly correlates with the impedance. On core Sils13_2 the correlation is more difficult due to less characteristic changes in seismic and lithological facies. A transformation of two way travel time (twt) into depth with a constant velocity of 1450m/s enables a direct comparison of core and seismic data. The thickness of the different units was calculated by subtracting the depth of the lower horizon from the upper horizon on every shot point (see results in Section 4.2 Figures

26 to 35).

3.4.4 Interpolation for isopach maps

The thickness of the sediment packages was interpolated based on the calculated thicknesses along the seismic lines (Figures 26 to 35). The results of interpretation are described in Section 5.1 on Page 40). The interpolation and interpretation was made manually with Adobe Illustrator. Volume calculations were performed with Esri ArcGis and IHS Kingdom Suite but did not produce satisfactory results due to gaps in the data and additional sediment processes.

Differences in thickness, where different seismic lines crossover, occur due to different local velocities, imprecise GPS positioning, lacking seismic resolution and the time span between this study and Blass et al. (2005). In this case the average thickness was taken. Higher sedimentation rates are interpreted in depressions on the ancient lake floor (see Figure 34 as an example of sediment thickness variations).

Below the gas covered sections depressions are expected. Therefore thicker sediment infillings were inferred in these areas. An example of such a depressions and the resulting uncertainties is shown in Figure 29 on Page 31. Here the side walls of the depression show dipping slopes with no evidence for the total depth of the depression. The interpretation of these depressions is very speculative. On the side walls of the Maloja Basin likely low sedimentation rates predominate due to only fine and biogenic sediment input. Basinal current deposits can be excluded (Lehman, 1975; Sturm & Matter, 1978; Schnellmann et al., 2006). Additionally local high sedimentation rates are expected near the smaller inlets of the Lake (see Figure 3). Blass et al. (2005) also considered these two effects.

Small scale variations in the sediment distribution are generalized to the scale of interpretation.

3.4.5 Calculation of denudation rates

The sediment thicknesses of the different units in core Sils13_1, as determined in Section 4.1, were extrapolated to sediment volumes based on a linear extrapolation of the calculated lake wide volume of $4.5*10^6\mathrm{m}^3$ for the time since the mass flow deposit (Unit 2) of Blass et al. (2005) for Unit 1 and described in Section 5.6. The sediment volumes were divided by the deposition time interval of each unit and the catchment area of Lake Sils to calculate the catchment wide denudation rate. The denudation rate was calculated with the assumption, the denudation in the catchment is homogenous, all the physical and chemical eroded material is deposited in Lake Sils and no antigenic sediment is produced and sedimented in the lake.

4 Results

4.1 Sediment Cores

The sediment of core Sils13_1 and Sils13_2 can be divided into 6 lithotypes (Figures 9 and 10). The characterization is based on visual description, MSCL measurements, thin sections, smear slides, coulometric measurements and XRF scans. Each lithotype is divided into subtypes. The Lithotypes are described in this section. A description of the Lithosubtypes and a detailed core description in 1m pieces is attached in the appendix. The color code of the lithotypes in the figures in this thesis is consistent with the colors in the detailed core description.

All the samples of the coulomat measurements are below 0.2% of inorganic carbon. This implies the carbonate content is 1% in maximum. Expect sample CG 48 with 0.68% which correspond to a carbonate content of 3.9%.

All elements, as derived from XRF core scanning correlate with the density expect Pb. The changes in density influence the elements differently. Pb is the only element which reacts anti-correlative to the density (see XRF results on Page xxxvii in the appendix).

4.1.1 Lithotype A

The diffusely laminated silt of Lithotype A contains mostly micas and quartz as inorganic components. Around 30% of the organic components are of diatoms and arthropods from the organic component of the sediment. The diatoms are representatives of the centric Cyclostella class in size of $10\mu m$ and the araphid Tabellaria species in size of $40\mu m$ (see Figure 12 and 13). The diatoms in core Sils13_2 are often bigger in size. The Aulacoseira class diatoms are especially large up to 0.1mm in width (see Figure 14). The top 5cm are characterized by a low bulk density of 1.1g/cm^3 to 1.3g/cm^3, a dark brown color and a organic carbon content of 3% on top and a content of 2% on 5cm core depth (see Figure 11). The Ba/Ti ratio peaks correlate with a increasing brown color. Lithotype A consists of 0.5% to 0.7% of organic carbon. A general decrease of organic carbon is recognizable totether with a decrease in brown tint and a increase in density down core. Both cores contain of reddish patches or horizons which were initially black and getting brighter after opening. This horizons or patches are of the same lithology as the surrounding sediment and an additional high content of organic matter.

A sharp contact on the transition of Lithotype A to B is in contrast to the diffuse gradual change in several pulses on the transition of Lithotype A to C.

The background sedimentation in interrupted by bright grey and brown interlayers. The bright
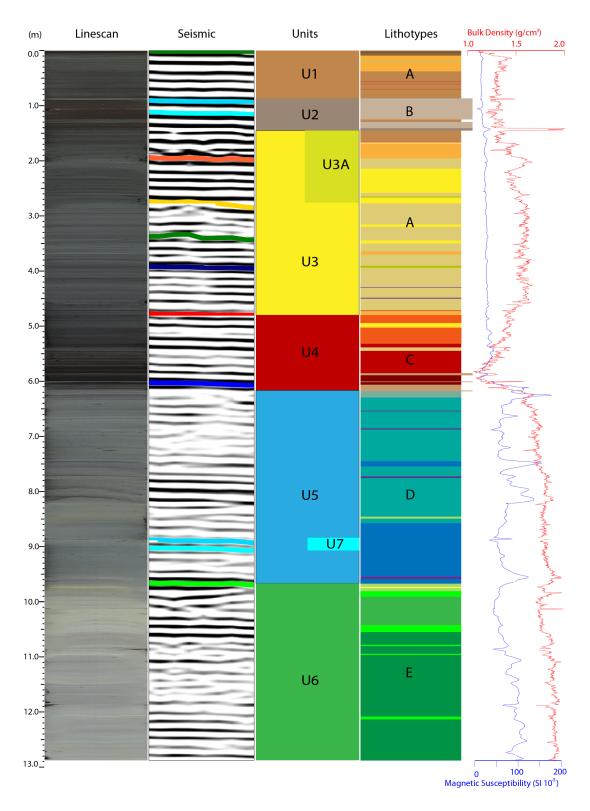
Figure 9: Composite section of core Sils13_1 with seismic units, lithotypes, seismic correlations and MSCL bulk density (red) and magnetic susceptibility (blue). The color legend of the lithotypes is indicated with a color box next to the corresponding subtype.
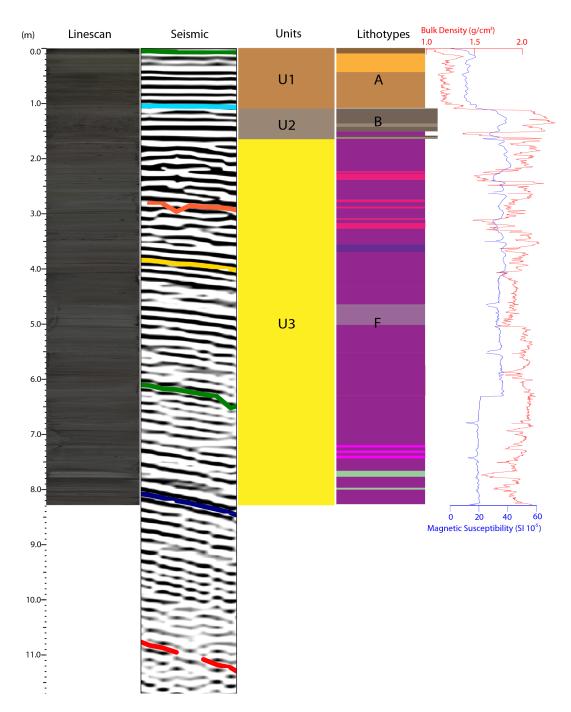
Figure 10: Composite section of core Sils13_2 with seismic units, lithotypes, seismic correlations and MSCL bulk density (red) and magnetic susceptibility (blue). The color legend of the lithotypes is indicated with a color box next to the corresponding subtype.

interlayers are clay rich and contain fewer diatoms, the darker layers are coarser in grain size and have a higher content of organic matter than the surrounding Lithotype A. The thicker interlayers show a normal grading grain size distribution and a whitish clay rich top.

Diffusely laminated dark olive grey clayey silt is found in two short intervals in core Sils13_2 on the very bottom of core Sils13_2 at 7.7m. Reddish (initially black) patches are present there.
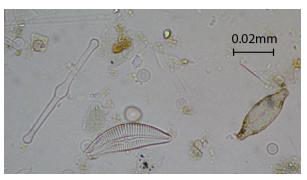
Figure 12: Diatoms in smear slide 7. On the left a long Tabellaria Fenestrata, on the right a Tabularia and in the center a item of the asymetrical Biralphid category. Several smaller centric diatoms of the Cyclotella class in the background.
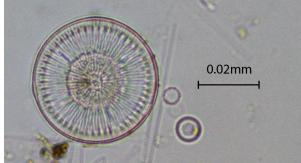
Figure 11: Line scan of dark layer at top of core Sils13_1 from section 1_7_sc four hours after opening

Figure 13: One item of a centric diatoms of the Cyclotella class found in smear slide 7

4.1.2   Lithotype B

Lithotype B is characterized by a brownish graded silt to fine sand sediment with a white top layer. The whitish top contains about 35% of clay fraction and no coarser grains than fine silt fraction (see Figure 15). The Fe counts of the XRF measurements peaks at top of the whitish top. The Al/Si ratio peaks on the top of Lithotype B. The majority of Lithotype B in core Sils13_1 is a homogenous sandy silt with a high organic carbon content of 3% as core Sils13_2 is of a fine to coarse sand and a organic carbon content of 0.2% to 1%. There quartz, chlorite, mica and amphibole grains occur with centric, araphid, asymmetrical biraphid and surirelloid diatoms. The large Aulacoseira class diatoms up to 0.1mm in radial diameter are abundant. The around 2.1 g/cm^3 dens base of Lithotype B is normal graded up to fine sand in core Sils13_1 and coarse sand in Sils13_2. Variations in clay content show a general decrease down core.
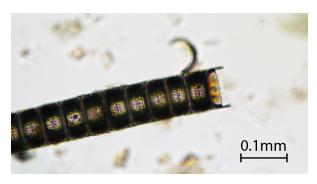
Figure 14: Diatom in smear slide 53b of core Sils13_2 and core section 2_2_b with a colony of Aulacoseira class diatoms.
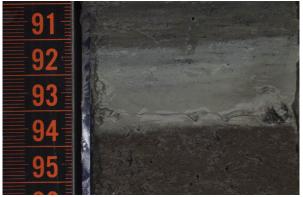
Figure 15: Line scan transition if A3 to B1 and B2 at the base of core Sils13_1 from section 1_7_sc four hours after opening.

4.1.3 Lithotype C

A diffusely laminated dark brown silt with a high organic carbon content and a high percentage of diatoms form Lithotype C. There are centric, araphid, asymmetrical biraphid, surirelloid diatoms and even the large centric Aulacoseira diatoms are abundant. The internal variations in brown color correlate with the organic carbon content. An increases in darkness down core corresponds to increasing carbon content from 1.5% to 3.6%, low density values down to $1.1g/cm^2$ and a high Mn/Fe ratio. Several grey clay interlayers interrupt the brown sediment 15. These clay layers show increased Ti counts as well as increased Al/Si ratio. The organic carbon content of the grey interlayers is at 0.3%. Three small sections show a fluidized structure and a mixing with the brown component of Lithotype C. (Figure 17). The transition to the Lithotype D is gradual in a range of 5cm in core Sils13_1.

4.1.4 Lithotype D

Lithotype D is a clastic laminated grey clayey silt with a few to no diatoms. The lamination shows an internal grading from a fine silt to a nearly pure clay and a mean thickness of 2mm to 2.2mm (see Figures 18 and 19). The mineral content is mostly quartz and chlorite, some amphiboles and other heavy mineral are found but cannot be distinguished due to grain size. The bulk density is around $1.9g/cm^2$. The counts of all elements are increased in contrast to Lithotype A and C. The organic carbon content is lowered to less than 0.2%. Brownish often graded interlayers occur as well as bright grey clay interlayers. The brown interlayers have the same amount of organic carbon as the background sediment and the grey clay interlayers. The grain size of the brown interlayers are up to fine sand in grain size whereas the thicker interlayers

Figure 16: Core scan of section 1_4_a 60cm-66cm with color variations of Lithotype C.

Figure 18: Thin section SDs3 on core section Sils13_1_4_c with sediment structure of lamination of Lithotype D. Lamination from silt (dark grey) to clay (brown).

Figure 17: Core scan of section 1_4_b 76cm-80cm with Subtype C4.

Figure 19: Core scan of section 1_4_c 54cm-57cm with lamination of Lithotype D.

are of coarser grain size than the thinner ones (Figure 20). A thickening of the lamination together with a yellowish color occur on the transition to Lithotype E. The transition is defined on the distinct five yellow laminas of Lihtotype E (Figure 21).

4.1.5 Lithotype E

Type E is the deepest observed lithotype of core Sils13_1. This greenish grey to yellowish grey diffusely laminated clay in the top meter with a transition to homogeneous grey clay in the lower part is free of diatoms and contains clay and fine silt. The lamination weakens while thickening downward up to 5cm in size. The organic carbon content is below 0.1%. A bulk density of 2.0g/cm^2 is nearly constant in Lithotype E. Grey clay and brownish silt interlayers interrupt

Figure 21: Core scan of section 1_5_c 83.5cm-89cm with color variations of Subtype D5 and the distinct five yellow laminas of Subtype E1.

Figure 20: Thin section SDs4 on core section Sils13_1_5_c with sediment structure of lamination of Lithotype D. Lamination from silt (dark brown) to clay (brown).

Figure 22: Mafic gravel piece found in pure clay at 10.105 meter core depth in core Sils13_1.
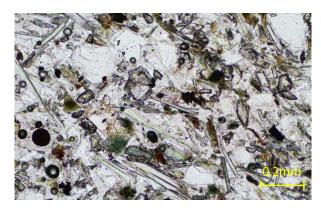
the background sedimentation in the laminated top and the diffusely laminated lower part of Lithotype E. The interlayers are around 1mm to 4mm thickness.
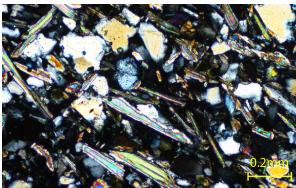
A gravel piece of 1cm in diameter was found at 10.105m depth in core Sils13_1, which is 40cm down from the top of Lithotype E, and this gravel piece is a dark green and fine grained aggregate of serpentine probably antigorite (see Figure 22). One core half from 10.43m to 10.53m depth of core Sils13_1 was washed through a $125\mu m$ sieve, 14 grains in a size between 2mm and 8mm in maximum diameter are found. Seven grains are greenschists with chlorite, felspars and quartz. Three grains are serpentinites, one contains a small pyrite. Mica gneisses and pure quartz grains are also present with two grains each. A sudden change in thickness of the lamination occurs at 10.50 meter sediment depth at core Sils13_1.

4.1.6   Lithotype F

Lithotype F is characterized by a diffuse laminated coarse silt to medium sand. The color varies in different olive grey and brownish grey tints. The relative high density of around $2.1g/cm^3$ and high rigidity are special for type F. The few diatoms are from the centric Cyclostella class in size of $10\mu m$ and the araphid Tabellaria in size of $40\mu m$ as in Lithotype A (see Figure 12 and 13). The organic carbon content is in a range of 0.2% to 0.8%. Minerals such as quartz, chlorite, muscovite, biotite are the major components in this lithotype. Riebeckite, actinolite, epidote, titanite, garnet, turmaline and calcite are found in the thin section SDs6 and SDs7 as minor component (Figures 23 and 24). The variations in XRF counts are of small amplitude in the whole Lithotype F. The background sedimentation is interrupted with dark brown interlayers. They are of the same grain size and composition as the background sediment. The amount of organic matter of these interlayers is in a range of 0.6%.

Figure 23: Thin section SDs6 on core section Sils13_2_2_c under plain polarized light in Subtype F1.

Figure 24: Thin section SDs6 on core section Sils13_2_2_c under cross polarized light in Subtype F1.

4.2   Seismic Units

Seven seismic units are distinguished due to their seismic facies in the survey of Lake Sils. The spatial distribution of the seismic units and their thickness is extracted from the data. Unit 7 was detected later and is within Unit 5 (Figure 25). The penetration depth of the seismic signal reaches depth of 30 meters in the Central and south-eastern part of the Maloja Basin. This corresponds to a two way travel time of 40ms. The penetration in the Central Basin as well as the Sils Basin and Lagrev Basin is restricted to maximum of 4 meters. The units in both cores are shown in Figures 9 and 10 on Page 20 and 21. The color of the seismic horizons is consistent in all seismic figures.
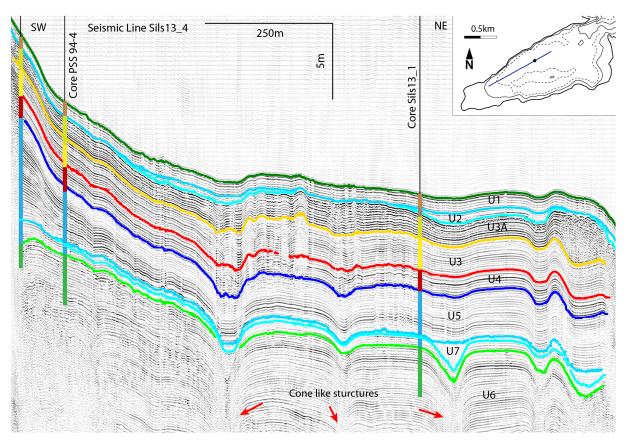
Figure 25: Seismic units on seismic line Sils13_4 with core location Sils13_1, PSS94-4 from Ohlendorf (1999), and profile on trace 2290.

4.2.1   Unit 1

Unit 1 is the uppermost unit. It shows clear reflections with a small decrease in amplitude downwards. A high amplitude reflector is situated right in the center of Unit 1. It shows a draping geometry and has a nearly constant thickness of about 1m over the Maloja Basin
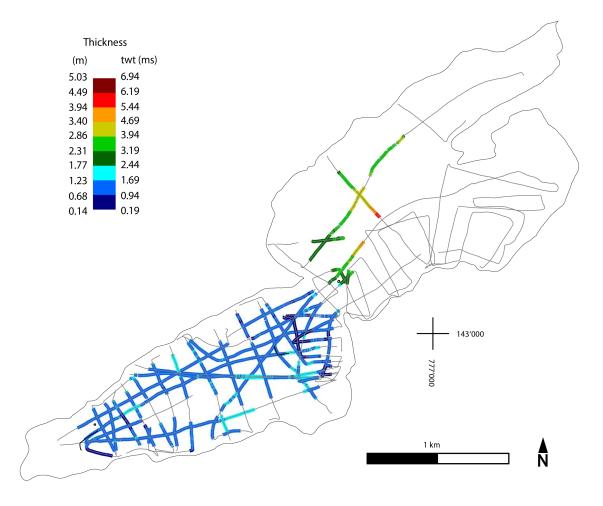
Figure 26: Thickness of Unit 1 on seismic lines. Thickness calculated with constant a constant velocity of 1450m/s.

(Figure 26). The seismic lines of this study give minor new information in the Central Basin area in comparison to Blass et al. (2005).

4.2.2 Unit 2

Unit 2 is seismically transparent and fills several depressions and thins out over ridges (Figure 27). The thickness is in a range of 0.15m to 1.5m in the Maloja Basin an up to 5m in the Central Basin. Clearly visible slide scars delimit Unit 2 (Figure 28). Whenever gas is present the seismic waves maximally penetrate Unit 2 (Figure 29).

28
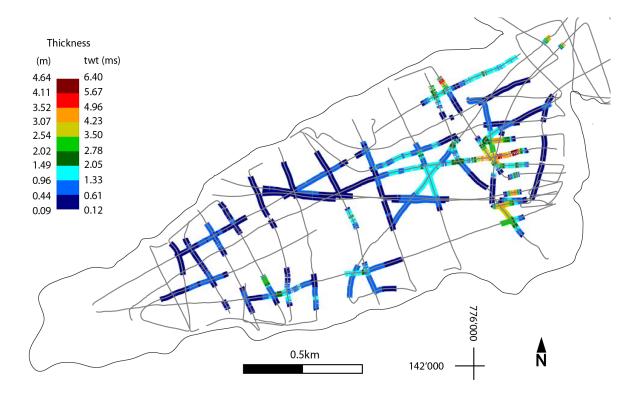
Figure 27: Thickness of Unit 2 on seismic lines in the Maloja Basin. Thickness calculated with a constant velocity of 1450m/s.
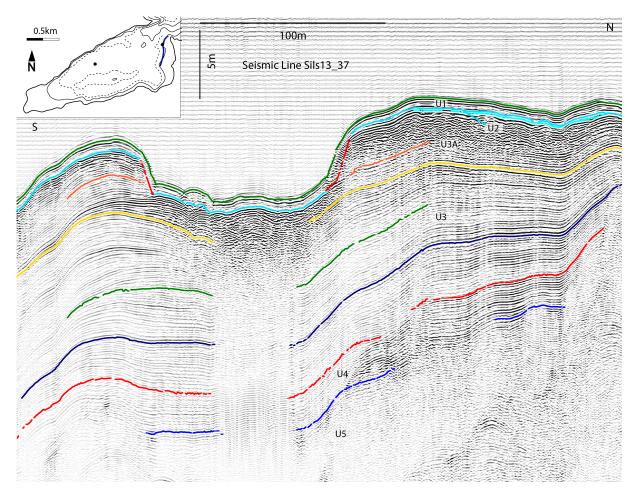
Figure 28: Seismic units on seismic line Sils13_37
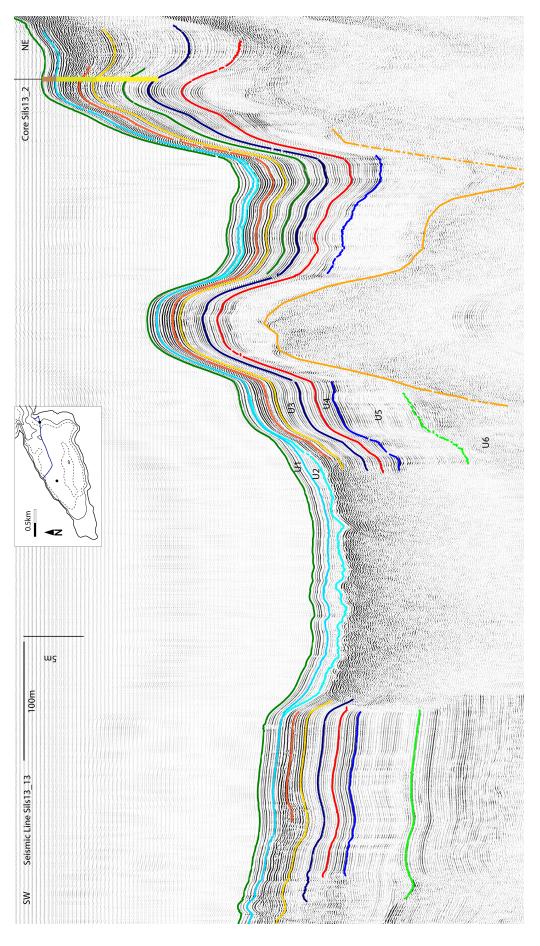
Figure 29: Seismic units on seismic line Sils13_13 near core location Sils13_2

4.2.3 Unit 3

Unit 3 shows strong regular reflections in the upper meter and normal amplitude reflections in the lower part with a relatively constant thickness in the Maloja Basin. A thickening towards the south-eastern end of the Isola Delta is observed (see Figures 30 and 31). Here the upper most part, Subunit 3A, shows a stronger input on the south edge of the Isola Delta, while the total unit shows an equal sediment distribution on the delta shore towards the Maloja Basin. Subunit 3A shows strong irregular reflections on to the Isola Delta shore. As an example see Figure 29 near core location Sils13_2. The sediments on the ridges are thinner than the fillings of depressions.
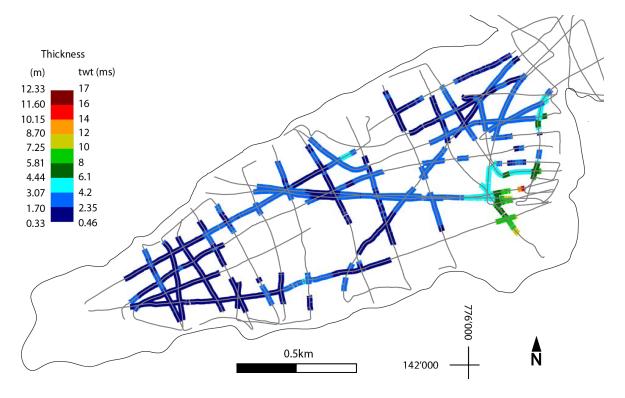
Figure 30: Thickness of Subunit 3A on seismic lines in the Maloja Basin. Thickness calculated with a constant velocity of 1450m/s.

4.2.4 Unit 4

The weak seismic reflectors of Unit 4 are limited by two strong reflections except for one high amplitude reflection in the center of the package. This unit shows a draping geometry and variations in thickness over the ridges and depressions but a thickening towards the Isola Delta (Figure 32). The thickness variations in the basin are of 30% in amplitude of the unit thickness and are concentrated to depressions like in the center of line 4 (see Figure 25).
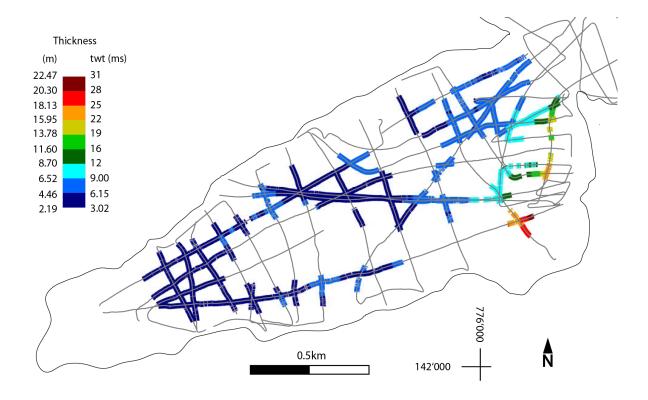
Figure 31: Thickness of Unit 3 on seismic lines in the Maloja Basin. Thickness calculated with a constant velocity of 1450m/s.
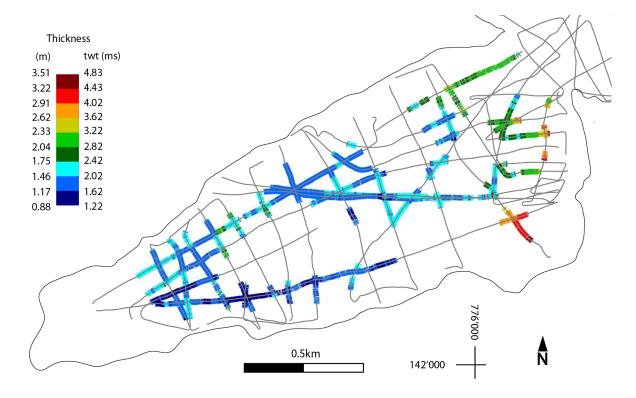
Figure 32: Thickness of Unit 4 on seismic lines in the Maloja Basin. Thickness calculated with a constant velocity of 1450m/s.
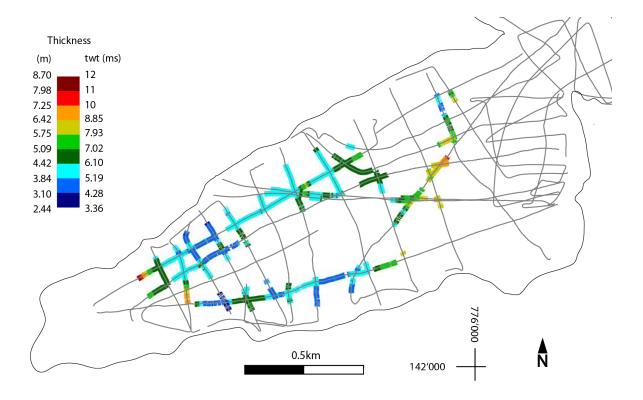
Figure 33: Thickness of Unit 5 including event of Unit 7 on seismic lines in the Maloja Basin. Thickness calculated with a constant velocity of 1450m/s.

4.2.5 Unit 5

Unit 5 shows weak seismic reflections with some distinct strong reflectors. The top 0.8m show a relative constant thickness over the Maloja Basin while the lower part of Unit 5 is spreading out towards the Isola Delta and the Maloja side of the lake (Figure 33). The stronger reflectors in the lower part at around 8m depth on core Sils13_1 split into two and three separate reflections towards the Maloja Basin. Unit 5 is the lowest unit and characterized by a draping behavior (Figure 34).
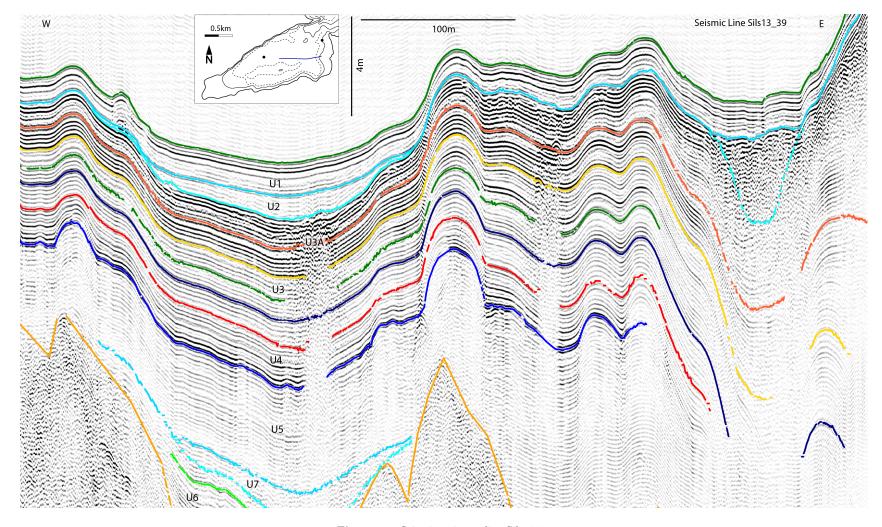
Figure 34: Seismic units on line Sils13_39
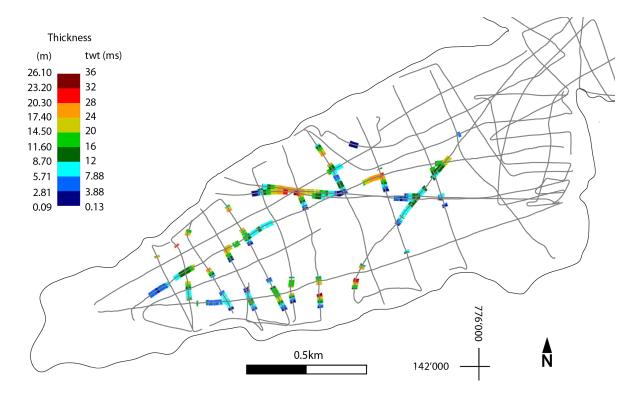
Figure 35: Thickness of Unit 6 on seismic lines in the Maloja Basin. Thickness calculated with a constant velocity of 1450m/s.

4.2.6   Unit 6

The deepest sediment unit of this study is Unit 6. This unit ponds onto the basement (Figure 35). The on-lap structures are visible for example on seismic line Sils13_13 (Figure 29) and seismic line Sils13_39 (Figure 34). The reflections are mostly weak except for a band of strong reflectors at the top of this unit. Several cone-like structures are recognizable in the lake (Figure 25). These structures are present in Unit 6 and terminate in Unit 5.

4.2.7   Unit 7

Unit 7 is seismically transparent, has a strong ponding behavior and spreads towards the edges of the central ridge in the Maloja Basin. It is situated in the basal part of Unit 5 and is visible only in the south-western part of the Maloja Basin (Figure 36).

4.2.8   Basement

The acoustic basement is a very irregular and chaotic reflector. The basement rock is not visible or recognizable over wide parts of the survey. A thinning of the sediment towards the basement
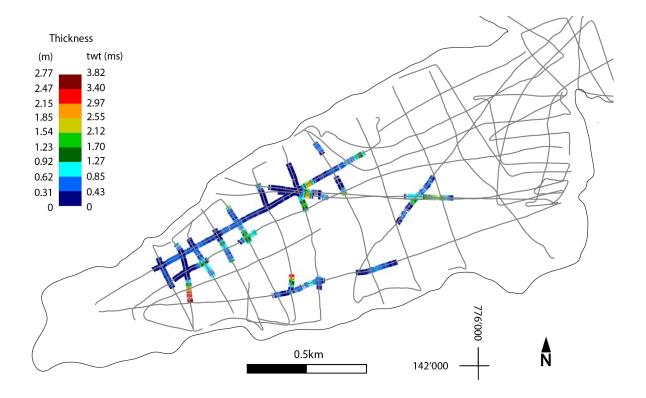
Figure 36: Thickness of Unit 7 on seismic lines in the Maloja Basin. Thickness calculated with a constant velocity of 1450m/s.

rock peninsula Piz d'Islas on the east shore of the Delta is observed (see Figure 28)

4.3   AMS C14 ages

Ten samples were measured in the AMS laboratory at ETH Hönggerberg in collaboration with Irka Hajdas. The results of the AMS measurements are listed in Table 5 and the results of the calibration are listed in Table 6. An interpretation of the ages and comparison with literature is described in Section 5.3 on Page 51. For the detailed calibration of used samples see Figures 76 to 85 in the appendix.

The sample Sils13_C14_5 was too small and lost during preparation. Sils13_C14_4 has a C14 age of 2501BP ±34 and Sils13_C14_6 has a C14 age of 1342 ±34, which is older than the age Sils13_C14_7. However in a continuous stratigraphy it is not possible to have an older age stratigrafically above a younger age. Therefore it was assumed, that these two C14 ages do not correspond to the sediment deposition age and that the samples have been reworked. With the age of Sils13_C14_10 being older than the age of Sils13_C14_2 reworking could also have played a role in this sample. Furthermore the age of Sils13_C14_2 is very close to the one of Sils13_C14_9. This short time span leaves nearly no time to deposit almost 4 meters of sediment (see age model

Table 5: C14 samples and results of AMS measurements (BP=1950AD)

Name	ETH number	Section number	Section depth (cm)	Master depth (mm)	Material	C14 age BP	Error ±1σ
Sils13_C14_4	ETH-53765	1_1_a	58.7	777	root	2501	34
Sils13_C14_6	ETH-55743	1_7_sc	85.5-89.9	830	needles	1342	28
Sils13_C14_7	ETH-55744	1_1_b	23.5-25.5	1279	needles	1103	28
Sils13_C14_1	ETH-53762	1_3_c	78.8	5373	bark	7157	35
Sils13_C14_9	ETH-55746	1_4_a	61-62	5709	needles	8733	38
Sils13_C14_3	ETH-53764	1_4_b	24.6-27.6	6137	seeds	10454	248
Sils13_C14_10	ETH-55747	1_4_b	31-32	6191	seeds	12150	210
Sils13_C14_2	ETH-53763	1_5_c	64.5-81.5	9597	seeds	9150	231
Sils13_C14_5	ETH-53766	2_5_c	43.8-45.4	7748	wood	-	-
Sils13_C14_8	ETH-55745	2_5_c	41.5-43.5	7727	seeds	3804	91

in Section 5.3). The error of the measurements on the AMS laboratory at Hönggerberg is $\pm 1\sigma$.
With IntCal 4.2.3 an additional error is added to a total $\pm 2\sigma$ error.

Table 6: C14 samples with calibrated ages and ranges (BP=1950AD)

Name	Ages cal BP		Calendar age	Range ±2σ		Probability
Sils13_C14_4	2740	2466	653	137	BC	95.4%
Sils13_C14_6	1306	1237	678.5	34.5	AD	86.7%
Sils13_C14_6	1205	1185	755	10	AD	8.7%
Sils13_C14_7	1064	952	942	56	AD	94.3%
Sils13_C14_7	944	938	1009	3	AD	1.1%
Sils13_C14_1	8028	7933	6030.5	47.5	BC	95.4%
Sils13_C14_9	9833	9558	7745.5	137.5	BC	88.8%
Sils13_C14_9	9888	9845	7916.5	21.5	BC	6.6%
Sils13_C14_3	12776	11397	10136.5	689.5	BC	95.4%
Sils13_C14_10	14955	13565	12310	695	BC	95.4
Sils13_C14_2	10890	9667	8328.5	611.5	BC	90.9%
Sils13_C14_2	11136	10973	9054.5	81.5	BC	4.5%
Sils13_C14_5	-	-	-	-		-
Sils13_C14_8	4437	3959	2248	239	BC	94
Sils13_C14_8	3952	3927	1989.5	12.5	BC	1.4

5 Discussion

5.1 Sediment units

The thickness of the seismic units is interpreted manually with Adobe Illustrator. For details to the method see Section 3.4.4. The age of the units is discussed in Section 5.3.

5.1.1 Unit 1

In Unit 1 the total thickness over the Maloja Basin is nearly constant which indicates a draping sedimentary process and no former event layers (Schnellmann et al., 2006). The fine sediment and constant thickness in the delta slope was deposited in a period of no considerable input from the Isola Delta. This unit was described precisely in Blass et al. (2005). Unit 1 is made up of Subtype A1 during a period of high biological production caused by anthropogenic influence, Subtype A2 by low production in the Little Ice Age and A3 with medium production in the Mediaeval Warm Period (Blass et al., 2005).
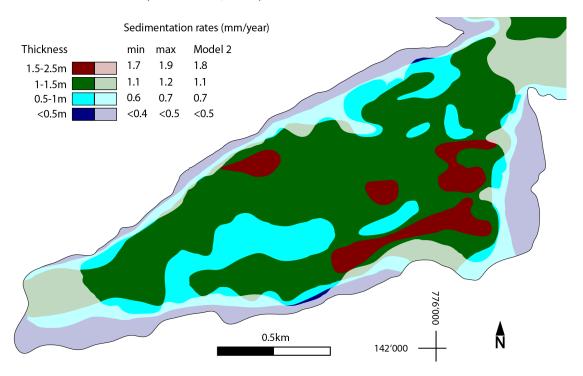
Figure 37: Interpolated isopach map of Unit 1 in the Maloja Basin, sediment thickness and sedimentation rates are based on the seismic and core data of this study, Blass et al. (2005) and age model 2 (see Section 5.3). The pale color shows area with no seismic data displayed in Figure 4.

The isopach map of Blass et al. (2005) is still valid in the Central Basin area. The changes of the map in the Maloja Basin area are minor (see Figure 37).

The now reddish patches in Lithotype A were initially black and brightened to the reddish tint during oxidization of iron mono-sulfides in contact with air (Kelts, 1978; Gilli, 2003). This indicates low oxygen conditions during deposition(Kelts, 1978; Gilli, 2003), even though the lake has a relatively low residence time and shows a dimictic behavior (Bosli-Pavoni, 1971). The microbiological activity in the buried sediment uses the available oxygen to degrade the abundant organic matter. This leads to the oxygen low conditions (Gilli, 2003).

5.1.2   Unit 2: Mass Transport Deposit 1

Unit 2 shows strong ponding structures (Figure 38). On the seismic lines multiple slide scars are recognizable (Figure 28). The ponding and basin infilling is typical for basal current transport processes such as turbiditic flows (Sturm & Matter, 1978). B1 is interpreted as a clay cap. An increased Fe content on top of the clay cap was also observed but not further discussed in Wirth (2013). The multiple slide scars and ponding behavior indicate multiple synchronous events (Schnellmann et al., 2006) which are seismically not distinguishable in Lake Sils. Two single events with a 5cm sediment of Lithotype A3 in between are found in the cores. The short gravity cores of Blass et al. (2005) do not reach a second event although in core PSS94-4 from Ohlendorf (1999) where two clay layers were recognizable.
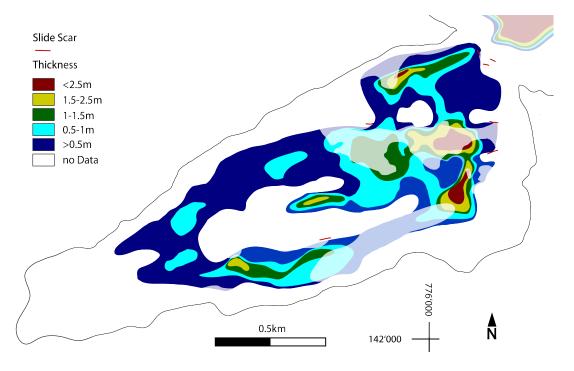
Figure 38: Interpolated isopach map of Unit 2 in the Maloja Basin, sediment thickness is based on the seismic and core data of this study and Blass et al. (2005). The pale color shows area with no seismic data displayed in Figure 4.

It cannot be distinguished which scar (Figure 38) and deposit leads to which event. The several slide scars indicate a lake wide process as trigger such as an earthquake or tsunami due to rockfall. As no former rockfall is known in the Maloja Basin area, an earthquake trigger is the more likely scenario dependance to Strasser et al. (2006).
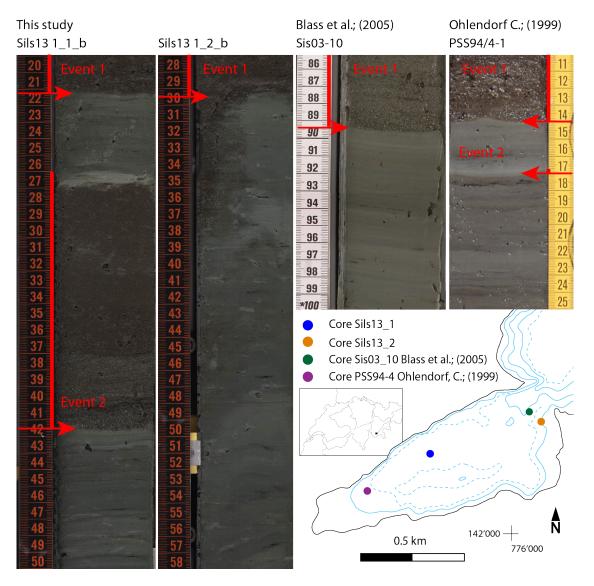
Figure 39: Base of Unit 2 in comparison with section 1_1_b and 1_2_b of this study with core Sis03-10 of Blass et al. (2005) and PSS94/4-1 of Ohlendorf (1999).

Additionally debatable is whether there are two events in Unit 2. A comparison of the base of Unit 2 on different core sections in Lake Sils is shown in Figure 39. The base of core section 1_1_b shows an undisturbed section with two different events with a clay cap each (marked with red arrows in Figure 39). Section 1_2_b show a disturbed base of only one layer. Of the short gravity cores of Blass et al. (2005) is only core Sis03-10 which could reach a second event on the base of Unit 2, but this core shows now second event. Core PSS94/4-1 of Ohlendorf (1999) shows

42

a bright clay layer at 17cm depth which can be correlated with the clay cap of a lower event. There is no singular solution and only a further sediment core would allow a final conclusion.

5.1.3 Unit 3
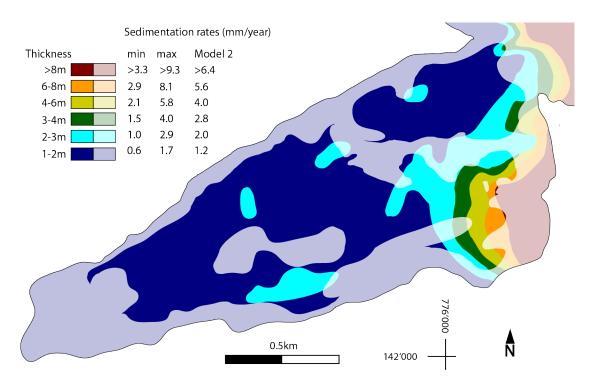
Figure 40: Interpolated isopach map of Subunit 3A in the Maloja Basin, sediment thickness and sedimentation rates are based on the seismic and core data of this study, Blass et al. (2005) and age model 2 (see Section 5.3). The pale color shows area with no seismic data displayed in Figure 4.

The sediment of Subunit 3 has its major source from the shore of the Isola Delta (see Figures 40 and 41). The sediment distribution of the draping clastic input is thinning towards the basin. The thickness variations on the other hand indicate the amount of ponding sedimentation processes like flood layers or turbiditic flows contributing to the total geometry. Unit 3 has a down core decreasing organic carbon content indicating decreasing biological production, with a reverse of the trend towards Unit 4. Lithotype A2 is reoccurring at the transition to Unit 4 which indicates a change in the depositional setting. The small variations in color and composition as well as XRF counts are a product of these changes in depositional environment. Subunit 3A indicates coarse input towards core location Sils13_2 which is consistent with the sedimentological observations. The coarse sediment of Lithotype F in core Sils13_2 indicates a period of high input from the Isola Delta in contrast to the fine sediment of Unit 1 at the same location (see Section 4.1). Unit 3, at least the segment sampled with core Sils13_2, represents a time of massive input
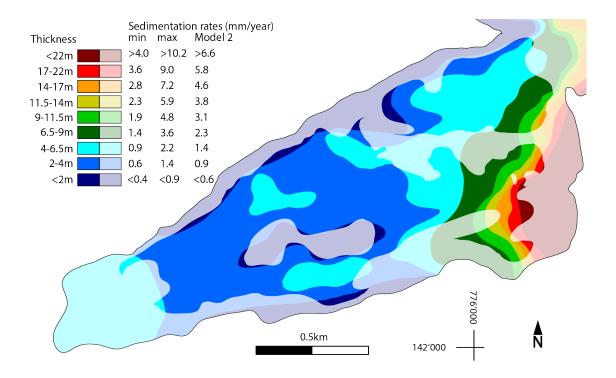
Figure 41: Interpolated isopach map of Unit 3 in the Maloja Basin, sediment thickness and sedimentation rates are based on the seismic and core data of this study, Blass et al. (2005) and age model 2 (see Section 5.3). The pale color shows area with no seismic data displayed in Figure 4.

from the Isola Delta towards the Maloja Basin. Subtype F6 at the base of core Sils13_2 indicates two short periods without considerable sedimentation towards the Maloja Basin. Although the Isola Delta delivered sediment into the Maloja Basin during the period of Unit 3, no distinct change in the lithological composition or grain size is recognizable in core Sils13_1. Hence it can be assumed that the sediment at this site is not considerably affected by the delivering direction of the Aua da Fedoz on the Isola Delta.

5.1.4   Unit 4

The sediment in Unit 4 has low clastic influence and is a mixture of about 70% draping and 30% ponding sediment (Figure 42). Events many are small and made up of a grey clay composition in contrast to the organic rich background sediment. These events are most probably responsible for thickness variations far below seismic resolution. A thickening towards the Isola Delta is present in this unit indicating the Val Fedoz as major tributary for the Maloja Basin. The higher amounts of organic matter and less terrestrial input corresponding to a high Mn/Fe ratio indicate a high productivity period with low catchment erosion (Leemann & Niessen, 1994). The density reduction in Unit 4 correlates with a lower clastic input into the lake, indicating a
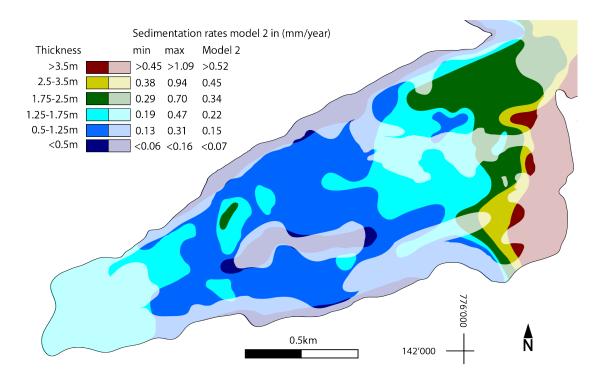
Figure 42: Interpolated isopach map of Unit 4 in the Maloja Basin, sediment thickness and sedimentation rates are based on the seismic and core data of this study, Blass et al. (2005) and age model 2 (see Section 5.3). The pale color shows area with no seismic data displayed in Figure 4.

catchment covered with more vegetation and a very small or absent glacier (Leemann & Niessen, 1994; Avnimelech et al., 2001).

5.1.5   Unit 5

The grain size distribution of the lamination in Unit 5 is characteristic for clastic varves (Hsü & McKenzie, 1985). The several smaller internal graded layers are high precipitation events in the catchment while every clay layer indicate a freezing of the lake in winter (Hsü & McKenzie, 1985). These varves are counted and discussed in Section 5.3. The draping geometry indicates a distal environment in respect to the glaciers (Figure 43). A ponding geometry would be expected in a proglacial lake with a glacier in a proximal position (Anselmetti et al., 2007). Unit 5 is interpreted to be a paraglacial phase in order to Slaymaker (2009) Unit 5 is thickening toward Maloja and the Isola Delta in contrast to the upper 4 units. This indicates a strong input of the Inn river or a melt water transport of the Forno glacier over the Maloja pass during this period, which reached down to Maloja Dorf at Egesen stage (Maisch, 1992) (see Figure 2). By suggesting the Forno glacier as a major tributary it would require a sudden change in sediment type in a core depth around 7.5 meter in core Sils13_1. However no change in lithology, lamination
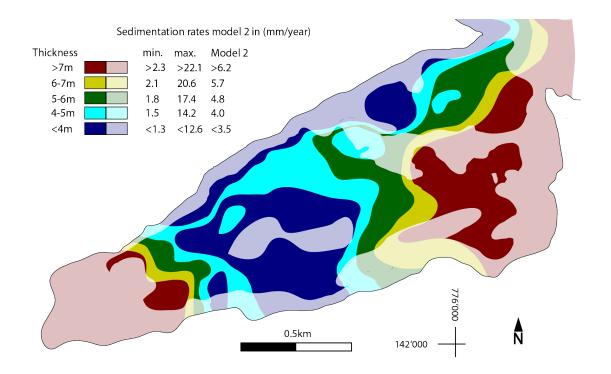
Figure 43: Interpolated isopach map of Unit 5 in the Maloja Basin, sediment thickness and sedimentation rates are based on the seismic and core data of this study, Blass et al. (2005) and age model 2 (see Section 5.3). The pale color shows area with no seismic data displayed in Figure 4.

thickness or event frequency has been detected. The high amplitude reflections correspond to flood events coming from the Maloja shore. This is visible in a comparison of core PSS94-4 from Ohlendorf (1999) and Sils13_1.

5.1.6   Unit 6

The sediment characteristics and the abundance of single coarse grains together with a ponding sediment structure is typical for a sediment formed in a proglacial environment (see Figure 44). The most reliable source of single sand grains and pebbles are icebergs from a glacier which is situated close to the lake (Bennett et al., 1996). Unit 6 fills the lake down to the acoustic basement or the limits of seismic penetration.

The serpentinite grains found during the sieving in Subtype E2 originate from the Platta nappe or Malenco unit. It is not clear whether they were delivered from the Forno valley or the Lägh dal Lunghin (see Figure 1).

The thickening down core of the lamination at the transition of Unit 5 to Unit 6 is interpreted as increasing sedimentation rate. The sudden change in lamination thickness coincides together with the three strong reflections in Unit 6.

46
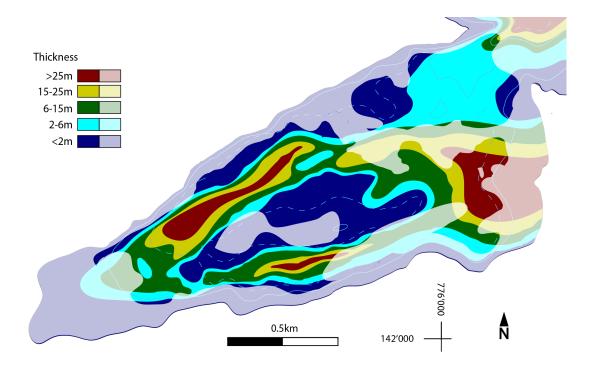
Figure 44: Interpolated isopach map of Unit 6 in the Maloja Basin, sediment thickness is based on the seismic and core data of this study and Blass et al. (2005). The pale color shows area with no seismic data displayed in Figure 4.

The cone like structures starting in Unit 6 are interpreted as pockmarks (marked with red arrows in Figure 25 on Page 27). With a diameter of up to 50m they are of medium size and are all relictic. They occur due to gas escape of a geologic or biogenic source (Pickrill, 1993; Duck & Herbert, 2006). Due to no organic material in Unit 6 a biogenic source is less likely.

5.1.7   Unit 7: Mass Transport Deposit 2

This unit is a smaller mass flow event which is made up of several mass flow deposits around the central ridge of the Maloja Basin and fillings of local depressions (Figure 45). Unit 7 and Unit 2 are a mass transport deposit and interrupt the background sedimentation of Lake Sils. No mass transport deposit sediment corresponding to Unit 7 was found in core Sils13_1. An evaluation of the extent of the mass flow is not possible with the present data set. The several mass flow deposits, even on both ridge sides in the Maloja Basin, indicate a lake wide process as trigger such as an earthquake or tsunami due to rockfall. As already mentioned in Unit 2 an earthquake is the most probable trigger for such a deposit. An increased earthquake activity after deglaciation due to post glacial rebound movements could be a trigger of this event Arvidsson (1996). Further studies show that increased seismicity is limited to local weakness zones such as the Engadin fault (Mazzotti et al., 2005). Due to the small number of events in Lake Sils this

47
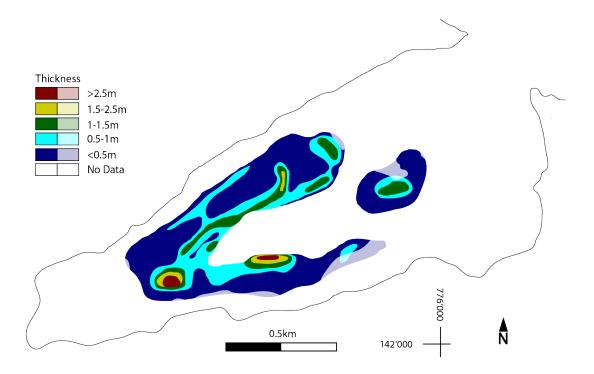
**Figure 45:** Interpolated isopach map of Unit 7 in the Maloja Basin, sediment thickness is based on the seismic and core data of this study and Blass et al. (2005). The pale color shows area with no seismic data displayed in Figure 4.

theory cannot be proven. This study will not further investigate this controversy.

5.1.8   Basement

The basement is not well observed with the current seismic survey. The valley form and the exposure of bedrock as the Piz d'Islas indicate an elongated glacial carving of the basin. Furthermore the isopach map of Unit 6 (Figure 44) indicates such an origin.

5.1.9   Events

Next to the two major mass transport deposits in Lake Sils defined as Unit 2 and Unit 7, several smaller events interrupt the background sedimentation. The several bright and dark interlayers are interpreted as mass transport deposits and flood layers. They appear in Lithotype A and F as brownish coarser layers or of grey clay composition. In Lithotype C, D and E the interlayers are of grey clay composition. The normal grading of the thicker event layers indicates a single mass transport event. An elevated amount of organic matter and organic carbon suggests also a terrestrial source (Adams et al., 2001).

5.2 Sediment distribution

5.2.1 Water currents

The combined line A1 indicates an area of nearly no sediment on the central ridge of the Maloja Basin (Figure 46). The sedimentary structures climbing from the north toward the top indicate a sediment transport due to currents which are also described in Blass et al. (2005). The top of the central ridge in the Maloja Basin is free of sediment indicating water currents during the whole holocene. The sediments of Unit 5 show onlap structures to the ridge. The sediments of Unit 4 rise up the highest onto the ridge. A change in geometry starts with onlap structures on the purple horizon indicated with red arrows in Figure 46. A clear correlation of the purple horizon with the red horizon is not possible due to incoherent seismic reflectors. Extrapolation leads to the interpretation that the purple horizon is of the same age as the red horizon, which indicates the change of Unit 4 to Unit 3. The changes in sedimentation are interpreted to be caused by changes of the lake current system. This changes could have their origin in a change of the border due to growth of the Isola Delta, closure of the passage on Sils Maria site, a change in water depth or water level variations.
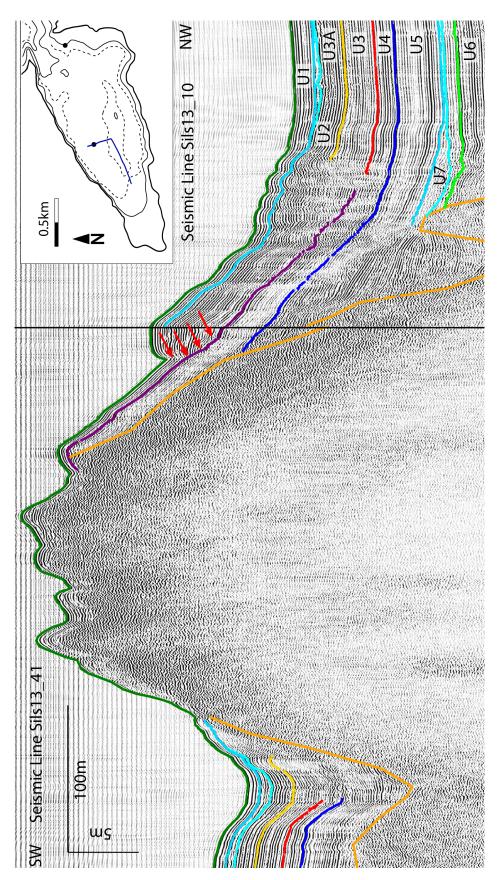
Figure 46: Seismic units on seismic line Sils13_10 and seismic line Sils13_41 on a combined seismic line (A1). Top lap structures marked with red arrows. The pale color shows area with no seismic data displayed in Figure 4.

5.3 Age model

5.3.1 Core Sils13_1

The measured and calibrated C14 ages are plotted in Figure 47. For the conflict with two oldest samples Sils13_C14_3 and Sils13_C14_2, at the top and bottom of Unit 5, there are three possible age models. In age model one sample Sils13_C14_2 is too young. A contamination of the very small samples measured with the gas method is more probable than for the other samples. This would lead to an old age for the Unit 5 in model one.

The second solution is that these two ages were swapped in the lab. A correction of the label on the sample tube of sample Sils13_C14_3 is indicates such a possibility which cannot be excluded or reconstructed. This age model is shown in Figure 48. According to Howarth et al. (2013) the best fit line in model 2 is younger than the measuring C14 error of sample Sils13_C14_9. The third solution is that sample Sils13_C14_3 was reworked, but this would be in conflict with the samples in Unit 4 and the varves in Unit 5. This model is not shown in the age model.

The probable range of the age model is based on the sedimentological observations and the error bars of the C14 ages. No input from the Isola Delta to the Maloja Basin in Unit 1 and sediment input from the Delta in Unit 3 is indicated in the grain size distribution in core Sils13_2. From these observations a higher sedimentation rate in Subunit 3A than in Unit 1 can be expected. Unit 4 indicates a low sedimentation rate of 0.2mm/year which is four times lower than the present day rate after Blass et al. (2005) and 10 times lower than the rate inferred from the varve counting in Unit 5. A comparable sedimentation rate in the upper half as in the lower half of Unit 4 is expected. The rhythmic lamination is interpreted as varves because of the sedimentary structure and the calculated sedimentation rate in the core, although there is no absolute C14 age to validate the time span of the varves. However there is no certain proof that the rhythmic laminations in Unit 5 are indeed varves or just several flood events with a high clay content on top of the lamination.

Lake Silvaplana also has a unit of organic carbon rich sediment with a low sedimentation rate and a transition to clastic organic carbon poor rhythmic sediment in the unit underneath (Leemann & Niessen, 1994). A comparison of the sediment description of Lake Silvaplana after (Leemann & Niessen, 1994) and the sediment of Laks Sils in this study indicate and similar climate and sediment history. The transition from Unit 5 to Unit 4 is dated to 9415 ±90BP C14 age (Leemann & Niessen, 1994). This age is calibrated to 10709 ±441BP and shown in Figure 48
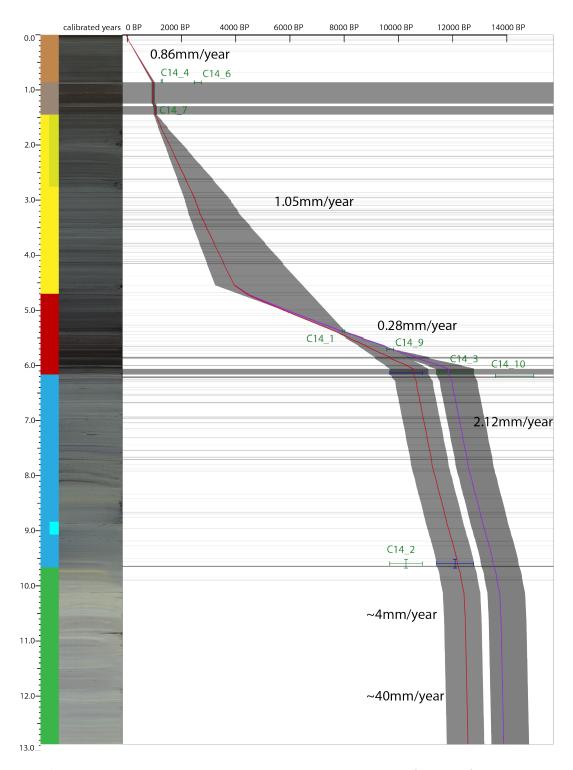
Figure 47: Age model of core Sils13_1. The measured and calibrated C14 samples (dark green) with model version 1 (purple) and its supposable range, switched samples (blue) with model version 2 (red) and its supposable range. Dark grey are events.

(details about the calibration see appendix).

The moraine on the shoulder of the Val Fedoz assigned to the Egesen stage indicates a proglacial
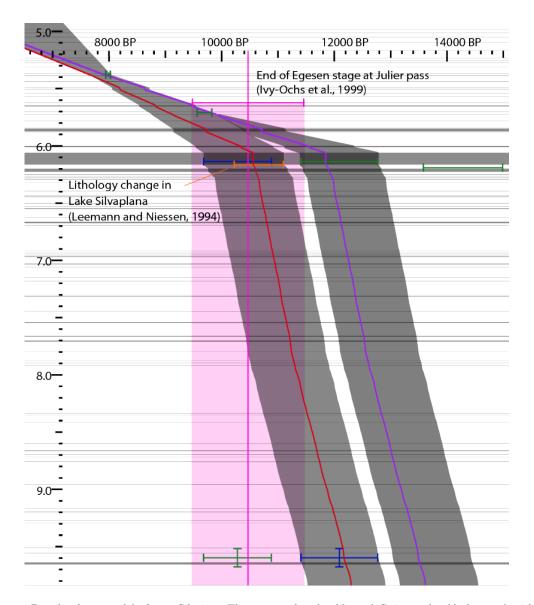
Figure 48: Details of age model of core Sils13_1. The measured and calibrated C14 samples (dark green) with model version 1 (purple) and its supposable range, switched samples (blue) with model version 2 (red) and its supposable range. Additional C14 age of Leemann & Niessen (1994) and exposure age based on ^{10}Be cosmogenic nuclides of Ivy-Ochs et al. (1999)

setting of Lake Sils during the Younger Dryas period (Maisch, 1992). The Egesen stage in the Upper Engadin was dated at Julier Pass, 10km north of Lake Sils, to 10470 (Ivy-Ochs et al., 1999). As a conclusion Unit 5 is thought to be related to the Younger Dryas stage. As an assumption of these correlations age model 2 is the most favorable.

5.3.2   Core Sils13_2

Only one sample was measured in core Sils13_2. The age of Unit 2 was correlated to age model of core Sils13_1 (see Figure 49). This results in a core base age of 4380BP. The sedimentation
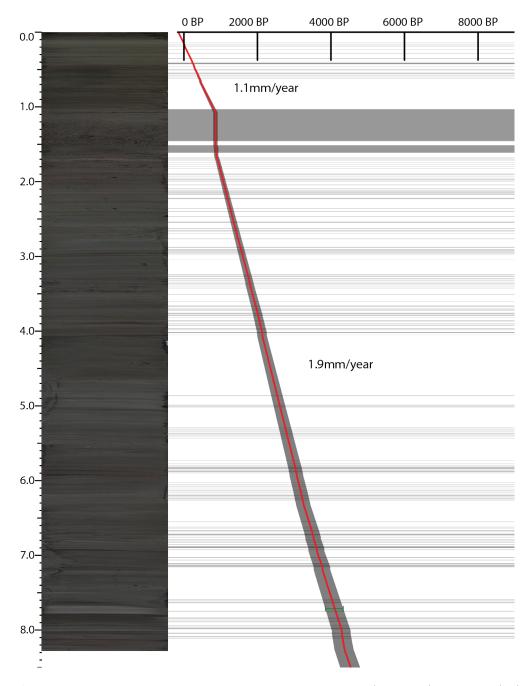
Figure 49: Age model of core Sils13_2. The measured and calibrated C14 sample (dark green) with model (red) and its supposable range.

rates in Unit 1 is 1.1mm/year, in the complete Unit 3 1.9mm/year. In the lower part of the core an increased sedimentation rate is observed. The sediment description indicates higher rates in Unit 3 than in Unit 1 which is consistent with the age model even though the uncertainty is still considerable.

5.4   Sedimentation rates

Due to the two favorable age model solutions two sedimentation rate distributions were created for core Sils13_1 (see Figure 50). Within the age model a large variation of the sedimentation rates is presented as possible. The extreme values are not very realistic. The sedimentation rate of Unit 1 is calculated to a range of 0.8mm/year to 1mm/year which is comparable to the sedimentation rates from Blass et al. (2005). The rate in Unit 3 is somewhat higher than in Unit 1 due to the sediment characteristics. A minimum rate of Unit 3 is given by the C14 ages. Unit 4 is low in each possible model, so the general trend in the section remains the same.
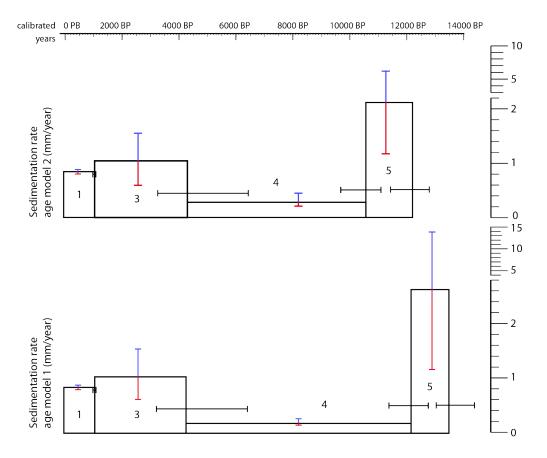
Figure 50: Comparison of sedimentation rates of age model 1 and 2 with the four units is side the age model with the possible variation inside of the supposable range indicated with the grey bar in Figure 47

The relatively high rate and uncertainties of the C14 ages in Unit 5 enable short sedimentation periods and results in extremely high rates (Figure 50). Due to the sediment structures indicating varves in Unit 5 the sedimentation rate is most favorable in a range of the varves around 2.0mm/year to 2.2mm/year.

The calculated sedimentation rates of all units give no evidence for neither of the two age models.

Figure 51: Comparison of sedimentation rates of different locations, based on Core Sils13_1 of this study, PSS94-4 from Ohlendorf (1999) and two profiles based on seismic line Sils13_4 and Sils13_5.

The comparison of the different sedimentation rates on specific sections in the Maloja Basin show the increasing sedimentation towards the deltas of the Lake, as expected (Figure 51). The shape of the bedrock has a large influence on the sedimentation rate distribution in the lake. Trace 3400 on line Sils13_5 indicates a higher sedimentation rate in Unit 3 in comparison to core Sils13_2, although trace 3400 is further away from the delta than core Sils13_2. Indeed the bedrock is rising towards the Piz d'Islas (see Figure 28 on Page 30).

A doubling of the sedimentation rate in a distance of 60 meter from core PSS94-4 to the profile along trace 2290 on line Sils13_4 is shown in Figure 51 and indicates a formation of a delta during the deposition of Unit 5. The general trend indicate a higher input in the cold phase Younger Dryas, a low input in the Holocene Thermal Maximum and a increased input in the Late Holocene.

5.5 Climatic correlation

The sedimentary record of Lake Sils and its inferred climatic driving force is in good agreement with other climate records of the Holocene time period. A high correlation is found with the flood frequency of the southern alps Wirth (2013). A high flood frequency indicates high precipitation or low vegetation cover (Wirth, 2013). A low sediment input in the time of 10k years to 4.5k years BP corresponds to a higher sediment yield from 4k to 2k years BP, indicating the warm
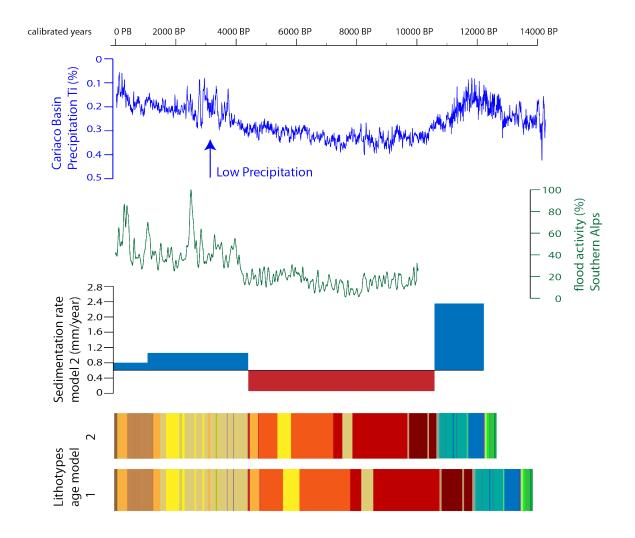
Figure 52: Comparison with Holocene climate records. Time dependent correlation with Ti counts of the Cariaco Basin in northern Venezuela Haug et al. (2001) and flood acclivity record of five south alpine lakes Wirth (2013). The Legend of the color bar of the lithotype record is listed in Figure 53 in the appendix on page viii.

period of the Holocene Thermal Maximum followed by a cold period with higher erosion. The increased sedimentation rate at 4.6k cal. year BP in this study is coinciding with negative temperature anomalies in Greenland, North America, Africa and Antarctica (Wanner et al., 2011). The end of the late glacial cold phase with several glacial advances at 3.2 cal. years BP (Schimmelpfennig et al., 2012) is coinciding with a change in lithology in core Sils13_1 to a higher organic component. The upper halve of Unit 1, sediment of Subtype A2 (indicated in bright brown in Figure 52), corresponds perfectly with the Little Ice Age in the flood activity record.

The climate record of the Cariaco Basin of (Haug et al., 2001) correlate with the South Alpine climate trend as already referred in Wirth (2013). The low Ti% values in the Cariaco Basin

record indicate low precipitation in northern Venezuela (Haug et al., 2001). A low precipitation record in the Cariaco Basin coincides with a cold climate on the Lake Sils area. A shift from the Younger Dryas period to the Holocene Thermal Maximum is indicated in the Cariaco Basin record as well as in the flood record in the Southern Alps. While warm conditions from 10k years to 4.5k years BP correspond with the brownish tint in the sediment record of Lake Sils, lithotypes indicating low biological production and high terrestrial runoff match the Cariaco Basin record. Even the gradual decrease of organic matter in the sediment of Unit 4 is corresponding to the Increased flood activity and the Ti counts in the Cariaco Basin.

A correlation with the holocene warm periods on the Tschierva glacier (Joerin et al., 2008) is roughly given with the Unit 4. Additionally the grey section in core Sils13_1 around 5.4m in Unit 4 correlate with the Kromer stage of Kerschner et al. (2006) in the same uncertainty as the Tschierva variations.

No correlation with the records of the Northern Alps (Wirth, 2013) or the Greenland ice core data (Mayewski et al., 1997) was found. In contrast to the most other European sites for the Holocene Thermal Maximum, Lake Sils follows a South Alpine trend starting around 10k years BP (Ilyashuk et al., 2011; Renssen et al., 2009).

The climate record indicate the glaciated area in the catchment as a major driving force for the sediment yield towards Lake Sils.

5.6 Sediment volumes in Lake Sils

The hypothesis that core site Sils13_1 is not affected by the delivery direction of the Isola Delta is sustained by the large distance to the Isola Delta where changes in coarse sediment do not reach site Sils13_1. Furthermore assuming today's currents to be valid for the entire time of the lake lead to a regular distribution of the fine sediment fraction. With these assumption changes in sedimentation rate in the Maloja Basin are only affected by the delivery variations.

With the assumption that core site Sils13_1 is not affected by the behavior of the Isola Delta the changes in sedimentation rate in core Sils13_1 are driven by changes in the sediment yield to the whole Lake Sils. Under the assumption the catchment denudate homogenous and the sediment yield to the lake is equal to the denudation rate in the catchment, the sediment volumes of the different units can be calculated to catchment wide denudation rates (Table 7). The calculated denudation rates indicate a 12 to 14 fold higher erosion rates during unit 6 than modern values. The time interval of unit 6 is based on the assumption one lamina is one year which results in a

Table 7: Table with linear calculated sediment volumes based on Blass et al. (2005), with linear extrapolation to a catchment wide denudation rate. (Details to the calculation see Section 3.4.5.

Unit	Thickness core Sils13_1 (m)	Volume (10^6m^3)	Time interval Age Model 2	catchment wide denudation rate mm/kyrs.
U1	865	4.50	1089	0.09
U2	585	3.04	0	-
U3	3350	17.43	3335	0.11
U4	1365	7.10	6688	0.023
U5	3501	18.21	1133	0.35
U6	3209	16.69	255	1.43
U7	-	-	-	-

sedimentation rate of 4mm/year in the upper most meter and 40mm/year in the lower 2.2 meter of core Sils13_1. Is purely speculative and lowers the expressiveness of the denudation rate value of Unit 6.

5.7   Comparison with paraglacial cycle

The model of the paraglacial cycle (Church & Ryder, 1972) indicates a increased sediment yield from the catchment right after glacial retreat and a decrease to a primary subaerial denudation rate with time after deglaciation. A comparison of the sedimentation rate in Lake Sils with the proposed sediment yield after deglaciation in a paraglacial cycle concept of Church & Ryder (1972) result in a good correlation with a high sedimentation rate in the lower Unit 6 with a decrease upward in the core. An inconsistency arises by the proposed influence of the Forno glacier system, the strong sedimentation rate changes in the section and the thickening upward of the varves in Unit 5. The uncertainties of the age model and variabilities in renewed or delayed sediment reworking after Ballantyne (2002) can have large influences of the sedimentation rates in Lake Sils in the Late Glacial and early Holocene. A large sediment trapping in the Holocene Thermal Maximum due to newly formed basins can be excluded due to the present day valley form. The rise in sediment yield of Unit 3 and 1 in comparison to Unit 4 can be explained with the cold phase of 4.6 cal. k years BP (Wanner et al., 2011) to 3.2 cal. k years BP (Schimmelpfennig et al., 2012) induced by a global climate change.

6 Conclusion

6.1 Sediment history of Lake Sils

The sediment characteristics and geometry indicate that Lake Sils was in a proximal position to the Fedoz glacier before the Egenen stage. Dropsones indicate a glacier terminating in the lake itself. In the Younger Dryas the lake was in a distal proglacial position with formation of clastic varves. The sediment geometry indicate a second major tributary from the Maloja side probably from the Forno system. The Holocene Thermal Maximum in the Upper Engadin region started immediately after the end of the Younger Dryas around 10.4k year BP. This value is consistent over several studies performed in the Southern Alps (Ivy-Ochs et al., 1999; Ilyashuk et al., 2011; Wirth, 2013). A precise comparison with climate variation in the Holovene Thermal Maximum like the Kromer stage and the Tschierva warm periods were not possible due to the low precision in the age model. Where a qualitative correlation of the record of Lake Sils is indicating these variation in the sediment characteristics of Unit 4. The Late Holocene in characterized of a glacial advance which is indicated in the increasing clastic components and the lowered organic components in the sediment. The grain size distribution in core Sils13_2 suggests that the depositional period of Unit 1, starting at 949 ±63AD, was the longest time period during which the Isola Delta delivered no sediment into the Maloja Basin, at least since the end of the Holocene Thermal Maximum. The delta collapse proposed by Blass et al. (2005) would have had a large impact on the delta geometry and prevented the Aua da Fedoz to deliver sediment to the southern part of the delta shore.

6.2 Sedimentation rates in a paraglacial cycle

The variations in sedimentation rate over the Holocene time period were analyzed in this study. Due to a lack of seismic data in the Central Basin area no real sediment budget has been established. Additionally, no information about the delta dynamics has been extracted from the seismic data. Core Sils13_2 didn't yield the expected information about sediment dynamics of the Isola Delta. Indeed only two mayor stages could be distinguished. Nonetheless the time series of the sedimentation rates at the core locations and the traces on seismic lines provided a comprehensive overview of the sediment dynamic of Lake Sils. They are consistent with the regional climate. However the record only faintly correlates with a sediment delivery curve in a paraglacial cycle model. The sediment record of this studs delivers only minor information about the deglaciation, especially about the time before the Younger Dryas, a concluding statement

can not be given. The data of this study lead to the assumption that the regional climate had a higher influence on the sedimentation rate than the paraglacial cycle during the Holocene.

6.3   Driving forces for sediment yield

The correlation with climatic data and comparison with the paraglacial cycle indicate a high influence of the regional climate for the sediment yield to Lake Sils. Especially the glaciated are in the catchment in one of the major factors of the sediment yield. A differentiation of the influence and variation of the Fedoz catchment in comparison to the total catchment of Lake Sils cannot be done based on the data of this study.

This study shows that Lake Sils has many different external influences to the sediment history during the Holocene. These are the delta dynamic of the Isola Delta, the possible influence of the Forno tributary in the Late Glacial as well as the lack of seismic data in the Central Basin. Theses additional influences complicate an estimation of sedimentation rates coupled with denudation rates during the Holocene. The importance of these external factors make a quantitative estimation almost impossible. However Lake Sils is a good example for the variability of regional climate regimes in a changing global climate.

7 Outlook

7.1 Improvement of the age model

The age model shows two main weaknesses. The C14 age samples Sils13_C14_1, Sils13_C14_3, Sils13_C14_8 and Sils13_C14_10 are all taken from the lower half of Unit 4. This enables a high variation of the sedimentation rate and the error is extrapolated. The transitional zone on top of Unit 4 holds the highest uncertainty in the upper part of core Sils13_1. A sample should be taken at the transition from Unit 3 to Unit 4 to minimize the error and constrain the sedimentation rate in these two units. Furthermore one sample on the basal parts of core Sils13_1 should be taken to confirm the hypothesis of the clastic varves and to decide between age model 1 and age model 2. The age model of core Sils13_2 should be combined with age model of core Sils13_1. This was not possible due to a delivery beyond the time frame of this thesis of the results from the samples Sils13_C14_8 and Sils13_C14_10.

7.2 Additional core and provenance study

An additional core should be taken to resolve the ambiguity of Unit 2. This core should be long enough to reach the base of the lower event. Cores in the Central Basin and around the Isola Delta will only reach an age of 3k to 5k years and will give no further information about the Late Glacial period. In the Lata Glacial period Lake Sils and Lake Silvaplana were connected. To analyze the history of the Deglaciation period a study with combination of glacial stages, limnological approach, volume calculations and provenance analysis in the whole area of the Upper Engadin lakes has to be applied.

7.2.1 Forno glacier as tributary in Late Glacial

To evaluate the Forno glacier as possible tributary of the Unit 5 sediments, provenance analysis needs to be performed. Andalusite from the contact metamorphic complex around the Bergell intrusion in the Forno catchment (Wenk, 1973) would indicative for a transport of meltwater over the Malojapass. A different approach to resolve the question would be zircon dating. The zircons in the Bergell intrusion are of Tertiary age around 35Ma to 30Ma whereas the zircons in the Austrolapine nappes are of pre-alpine age (Gulson & Krogh, 1973).

7.3 Comparison with ^{10}Be cosmogenic nuclides data

A comparison with the catchment wide denudation rates based on ^{10}Be cosmogenic nuclides will give information about the linkage of the source part to the sink part. The data of this study will provide informations about the coupling of the source and the sink in terms of the sediment yield, the time dependance and retention of loose material in the catchment.

Acknowledgements

First of all I would like to thank my supervisors Michael Strasser and Florian Kober for the possibility to do such a comprehensive project in a single master thesis. Furthermore, I thank Reto Grischott for the support and scientific collaboration. Thanks also to Lukas Glur and Robert Hoffmann for the support and organization in the field. Special thanks to Anna Reusch and Adrian Gilli for the assistance in the lab, Heinrich Horstmeyer for the Geophysical assistance, and Irka Haydas for the ^{14}C dating. Special thanks to Christian Ohlendorf and Alex Blass for the collaboration and the detailed data of their previous work on Lake Sils. Thanks to Christian Bigler for the remote determination of the Diatoms. Additionally all my study colleges especially Fränzi and Markus for their ideas and help with the small and bigger problems while working on a thesis. Special thanks to Célia Lukas for the massive improvements in language. And thanks to Roman Donau and Franziska Blattmann for the.

References

Adams, E. W., Schlager, W., & Anselmetti, F. S. (2001). Morphology and curvature of delta slopes in swiss lakes: lessons for the interpretation of clinoforms in seismic data. *Sedimentology*, *48*(3), 661–679.

Anselmetti, F. S., Bühler, R., Finger, D., Girardclos, S., Lancini, A., Rellstab, C., & Sturm, M. (2007). Effects of alpine hydropower dams on particle transport and lacustrine sedimentation. *Aquatic Sciences*, *69*(2), 179–198.

Arvidsson, R. (1996). Fennoscandian earthquakes: whole crustal rupturing related to postglacial rebound. *Science*, *274*(5288), 744–746.

Avnimelech, Y., Ritvo, G., Meijer, L. E., & Kochba, M. (2001). Water content, organic carbon and dry bulk density in flooded sediments. *Aquacultural engineering*, *25*(1), 25–33.

Ballantyne, C. K. (2002). Paraglacial geomorphology. *Quaternary Science Reviews*, *21*(18), 1935–2017.

Bennett, M. R., Doyle, P., & Mather, A. E. (1996). Dropstones: their origin and significance. *Palaeogeography, Palaeoclimatology, Palaeoecology*, *121*(3), 331–339.

Bierman, P. & Steig, E. J. (1996). Estimating rates of denudation using cosmogenic isotope abundances in sediment. *Earth surface processes and landforms*, *21*(2), 125–139.

Blass, A., Anselmetti, F. S., Grosjean, M., & Sturm, M. (2005). The last 1300 years of environmental history recorded in the sediments of Lake Sils (Engadine, Switzerland). *Eclogae Geologicae Helvetiae*, *98*(3), 319–332.

Bosli-Pavoni, M. (1971). Ergebnisse der limnologischen Untersuchungen der Oberengadiner Seen. *Aquatic Sciences-Research Across Boundaries*, *33*(1), 386–409.

Bronk Ramsey, C. (2013). Oxcal v. 4.2. 3.

Burga, C. A. (1997). *Geoökologische und klimamorphologische Untersuchungen im Alpenraum: Isola-Delta, Val Fedoz und Val Fex, Oberengadin, Kanton Graubünden;[Projektschlussbericht im Rahmen des nationalen Forschungsprogrammes" Klimaänderungen und Naturkatastrophen" NFP 31]*. vdf Hochschulverlag AG.

Chopra, S., Castagna, J., & Portniaguine, O. (2006). Seismic resolution and thin-bed reflectivity inversion. *CSEG recorder*, *31*(1), 19–25.

Church, M. & Ryder, J. M. (1972). Paraglacial sedimentation: a consideration of fluvial processes conditioned by glaciation. *Geological Society of America Bulletin*, *83*(10), 3059–3072.

Cornelius, H. P. (1935). *Geologie der Err-Julier-Gruppe. 1. Das Baumaterial (Stratigraphie und Petrographie, excl. Quartär)*. Dalp.

Cornelius, H. P. (1951). *Geologie der Err-Julier-Gruppe*. In Kommission bei A. Francke Ag.

Cuven, S., Francus, P., & Lamoureux, S. F. (2010). Estimation of grain size variability with micro x-ray fluorescence in laminated lacustrine sediments, cape bounty, canadian high arctic. *Journal of Paleolimnology*, *44*(3), 803–817.

Duck, R. W. & Herbert, R. A. (2006). High-resolution shallow seismic identification of gas escape features in the sediments of loch tay, scotland: tectonic and microbiological associations. *Sedimentology*, *53*(3), 481–493.

Einsele, G. & Hinderer, M. (1998). Quantifying denudation and sediment–accumulation systems (open and closed lakes): basic concepts and first results. *Palaeogeography, Palaeoclimatology, Palaeoecology*, *140*(1), 7–21.

Elsasser, H. & Boesch, M. (1991). *Beiträge zur Geographie Graubündens*. Die Tiefbohrung Sils im Oberengadin im Lichte der Glazialmorphologie. Jürg Sutter.

Federal Office of Meteorology and Climatology MeteoSwiss (2014). Climate normals segl-maria. www.meteoswiss.admin.ch.

Florineth, D. & Schlüchter, C. (2000). Alpine evidence for atmospheric circulation patterns in Europe during the Last Glacial Maximum. *Quaternary Research*, *54*(3), 295–308.

Gensler, G. A. (1978). *Das Klima von Graubünden: ein Beitrag zur Regionalklimatologie der Schweiz*. PhD thesis, Schweiz. meteorologische Zentralanstalt.

Geotek Limited (2013). MSCL Manual. www.geotek.co.uk.

Gilli, A. P. (2003). *Tracking late Quaternary environmental change in southernmost South America using lake sediments of Lago Cardiel (49 S), Patagonia, Argentina*. PhD thesis, ETH.

Gulson, B. & Krogh, T. (1973). Old lead components in the young bergell massif, south-east swiss alps. *Contributions to Mineralogy and Petrology, 40*(3), 239–252.

Hantke, R. (1983). *Eiszeitalter : die jüngste Erdgeschichte der Schweiz und ihrer Nachbargebiete.* Ott Verlag.

Haug, G. H., Hughen, K. A., Sigman, D. M., Peterson, L. C., & Röhl, U. (2001). Southward migration of the intertropical convergence zone through the holocene. *Science, 293*(5533), 1304–1308.

Herrmann, A. G. & Knake, D. (1973). Coulometrisches Verfahren zur bestimmung von Gesamt-, Carbonat-und Nichtcarbonat-Kohlenstoff in magmatischen, metamorphen und sedimentären Gesteinen. *Fresenius' Zeitschrift für analytische Chemie, 266*(3), 196–201.

Hinderer, M. (2001). Late Quaternary denudation of the Alps, valley and lake fillings and modern river loads. *Geodinamica Acta, 14*(4), 231–263.

Howarth, J. D., Fitzsimons, S. J., Jacobsen, G. E., Vandergoes, M. J., & Norris, R. J. (2013). Identifying a reliable target fraction for radiocarbon dating sedimentary records from lakes. *Quaternary Geochronology, 17*, 68–80.

Hsü, K. J. & McKenzie, J. A. (1985). Swiss lakes as a geological laboratory. *Naturwissenschaften, 72*(7), 365–371.

Ilyashuk, E. A., Koinig, K. A., Heiri, O., Ilyashuk, B. P., & Psenner, R. (2011). Holocene temperature variations at a high-altitude site in the eastern alps: a chironomid record from schwarzsee ob sölden, austria. *Quaternary science reviews, 30*(1), 176–191.

Ivy-Ochs, S., Schlüchter, C., Kubik, P. W., & Denton, G. H. (1999). Moraine exposure dates imply synchronous younger dryas glacier advances in the european alps and in the southern alps of new zealand. *Geografiska Annaler: Series A, Physical Geography, 81*(2), 313–323.

Joerin, U., Nicolussi, K., Fischer, A., Stocker, T., & Schlüchter, C. (2008). Holocene optimum events inferred from subglacial sediments at tschierva glacier, eastern swiss alps. *Quaternary Science Reviews, 27*(3), 337–350.

Johnson, T. C., Halfman, J. D., Rosendahl, B. R., & Lister, G. S. (1987). Climatic and tectonic effects on sedimentation in a rift-valley lake: Evidence from high-resolution seismic profiles, lake turkana, kenya. *Geological Society of America Bulletin, 98*(4), 439–447.

Kelts, K. R. (1978). *Geological and sedimentary evolution of Lakes Zurich and Zug, Switzerland.* PhD thesis, Diss. Naturwiss. ETH Zürich, Nr. 6146, 0000. Ref.: Hsü, KJ; Korref.: Trümpy, R.

Kerschner, H., Hertl, A., Gross, G., Ivy-Ochs, S., & Kubik, P. W. (2006). Surface exposure dating of moraines in the kromer valley (silvretta mountains, austria)-evidence for glacial response to the 8.2 ka event in the eastern alps? *The Holocene, 16*(1), 7–15.

Leemann, A. & Niessen, F. (1994). Holocene glacial activity and climatic variations in the swiss alps: reconstructing a continuous record from proglacial lake sediments. *The Holocene, 4*(3), 259–268.

Lehman, J. T. (1975). Reconstructing the rate of accumulation of lake sediment: the effect of sediment focusing. *Quaternary Research, 5*(4), 541–550.

LIMNEX (1994). Gewässerzustand und Gewässer- schutzmassnahmen im Oberengadin. *Bericht zuhanden des Amtes für Umweltschutz, Kanton Graubünden.*, 75.

Löwemark, L., Chen, H.-F., Yang, T.-N., Kylander, M., Yu, E.-F., Hsu, Y.-W., Lee, T.-Q., Song, S.-R., & Jarvis, S. (2011). Normalizing xrf-scanner data: a cautionary note on the interpretation of high-resolution records from organic-rich lakes. *Journal of Asian Earth Sciences, 40*(6), 1250–1256.

Maisch, M. (1992). *Die Gletscher Graubündens: Rekonstruktion und Auswertung der Gletscher und deren Veränderung seit dem Hochstand von 1850 im Gebiet der östlichen Schweizer Alpen (Bündnerland und angrenzende Regionen).* Universität Zürich-Irchel, Geographisches Institut.

Maisch, M., Haeberli, W., Frauenfelder, R., Kääb, A., & Rothenbühler, C. (2003). Lateglacial and holocene evolution of glaciers and permafrost in the val muragl, upper engadine, swiss alps. In *Proceedings of the 8th International Conference on Permafrost*, volume 2, (pp. 717–722). Balkema: Zurich.

Marguí, E., Queralt, I., & Hidalgo, M. (2009). Application of x-ray fluorescence spectrometry to determination and quantitation of metals in vegetal material. *TrAC Trends in Analytical Chemistry, 28*(3), 362–372.

Mayewski, P. A., Meeker, L. D., Twickler, M. S., Whitlow, S., Yang, Q., Lyons, W. B., & Prentice, M. (1997). Major features and forcing of high-latitude northern hemisphere atmospheric

circulation using a 110,000-year-long glaciochemical series. *Journal of Geophysical Research: Oceans (1978–2012), 102*(C12), 26345–26366.

Mazzotti, S., James, T. S., Henton, J., & Adams, J. (2005). Gps crustal strain, postglacial rebound, and seismic hazard in eastern north america: The saint lawrence valley example. *Journal of Geophysical Research: Solid Earth (1978–2012), 110*(B11).

Naeher, S., Gilli, A., North, R. P., Hamann, Y., & Schubert, C. J. (2013). Tracing bottom water oxygenation with sedimentary mn/fe ratios in lake zurich, switzerland. *Chemical Geology, 352*, 125–133.

Niederreiter, R. (2013). Uwitec. www.uvitec.at.

Ohlendorf, C. (1999). *High Alpine lake sediments as chronicles for regional glacier and climate history in the Upper Engadine, southeastern Switzerland.* PhD thesis, Swiss Federal Institute of Technology, Zurich.

Oldenburg, D., Scheuer, T., & Levy, S. (1983). Recovery of the acoustic impedance from reflection seismograms. *Geophysics, 48*(10), 1318–1337.

Pickrill, R. (1993). Shallow seismic stratigraphy and pockmarks of a hydrothermally influenced lake, lake rotoiti, new zealand. *Sedimentology, 40*(5), 813–828.

Reimer, P. J., Bard, E., Bayliss, A., Beck, J. W., Blackwell, P. G., Ramsey, C. B., Buck, C. E., Cheng, H., Edwards, R. L., Friedrich, M., et al. (2013). Intcal13 and marine13 radiocarbon age calibration curves 0–50,000 years cal bp. *Radiocarbon, 55*(4), 1869–1887.

Renssen, H., Seppä, H., Heiri, O., Roche, D., Goosse, H., & Fichefet, T. (2009). The spatial and temporal complexity of the holocene thermal maximum. *Nature Geoscience, 2*(6), 411–414.

Richter, T. O., Van der Gaast, S., Koster, B., Vaars, A., Gieles, R., de Stigter, H. C., De Haas, H., & van Weering, T. C. (2006). The Avaatech XRF Core Scanner: technical description and applications to NE Atlantic sediments. *Geological Society, London, Special Publications, 267*(1), 39–50.

Röhl, U. & Abrams, L. J. (2000). 11. high-resolution, downhole, and nondestructive core measurements from sites 999 and 1001 in the caribbean sea: Application to the late paleocene thermal maximum1.

Schimmelpfennig, I., Schaefer, J. M., Akçar, N., Ivy-Ochs, S., Finkel, R. C., & Schlüchter, C. (2012). Holocene glacier culminations in the western alps and their hemispheric relevance. *Geology, 40*(10), 891–894.

Schmid, S. & Froitzheim, N. (1993). Oblique slip and block rotation along the Engadine line. *Eclogae Geologicae Helvetiae, 86*(2), 569–593.

Schnellmann, M., Anselmetti, F. S., Giardini, D., & Mckenzie, J. A. (2006). 15,000 years of mass-movement history in lake lucerne: Implications for seismic and tsunami hazards. *Eclogae Geologicae Helvetiae, 99*(3), 409–428.

Slaymaker, O. (2009). Proglacial, periglacial or paraglacial? *Geological Society, London, Special Publications, 320*(1), 71–84.

Spillmann, P. (1993). *Die Geologie des penninisch-ostalpinen Grenzbereichs im südlichen Berninagebirge*. PhD thesis, Eidgenössische Technische Hochschule.

Spillmann, P. & Tromsdorff, V. (2005). *Geologische Atlas der Schweiz* (Atlasblatt 119 mit Erläuterungen ed.). Number Blatt 1277 Piz Bernina. Bundesamt für Wasser und Geologie, Bern.

Strasser, M., Anselmetti, F. S., Fäh, D., Giardini, D., & Schnellmann, M. (2006). Magnitudes and source areas of large prehistoric northern alpine earthquakes revealed by slope failures in lakes. *Geology, 34*(12), 1005–1008.

Sturm, M. & Matter, A. (1978). *Turbidites and varves in Lake Brienz (Switzerland): deposition of clastic detritus by density currents*. Wiley Online Library.

Suter, J. (1981). *Gletschergeschichte des Oberengadins: Untersuchung von Gletscherschwankungen in der Err-Julier-Gruppe*, volume 2. Geographisches Institut, Universität Zürich.

swisstopo (2014a). Geologischer Atlas der Schweiz. www.map.geo.admin.ch.

swisstopo (2014b). Primärflächen VETKOR25. www.map.geo.admin.ch.

swisstopo (2014c). swissALTI3D Reliefschatierung. www.map.geo.admin.ch.

Tibaldi, A. & Pasquare, F. A. (2008). Quaternary deformations along the 'engadine–gruf tectonic system', swiss–italian alps. *Journal of quaternary science, 23*(5), 475–487.

Tjallingii, R., Röhl, U., Kölling, M., & Bickert, T. (2007). Influence of the water content on x-ray fluorescence core-scanning measurements in soft marine sediments. *Geochemistry, Geophysics, Geosystems, 8*(2).

Trümpy, R. (1977). *The Engadine line: a sinistral wrench fault in the Central Alps.* Geological Society of China.

Vogel, H.-H. (1995). *Geomorphologische Kartierung sowie gletschergeschichtliche und geochronologische Untersuchungen im Val Fedoz.* PhD thesis.

Wanner, H., Solomina, O., Grosjean, M., Ritz, S. P., & Jetel, M. (2011). Structure and origin of holocene cold events. *Quaternary Science Reviews, 30*(21), 3109–3123.

Wenk, H. (1973). The structure of the bergell alps. *Eclogae Geol. Helv, 66*, 255–291.

Westerhold, T. (2003). *The middle Miocene carbonate crash: Relation to Neogene changes in ocean circulation and global climate.* PhD thesis, dissertation thesis, 151 pp, Univ. Bremen, Bremen, Germany.

Wirth, S. B. (2013). *The Holocene flood history of the Central Alps reconstructed from lacustrine sediments.* PhD thesis, Diss., Eidgenössische Technische Hochschule ETH Zürich, Nr. 20860, 2012.

Wohlwend, S. (2010). Shoreline deposits around lej da segl, traces of a prehistoric tsunami? Master's thesis, ETH Zurich.

Yilmaz, Ö. (2001). *Seismic data analysis*, volume 1. Society of Exploration Geophysicists Tulsa.

A Appendix

A.1 Lithotsubtype desctription

The description of the Subtypes is based on the description of the Lithotypes in section 4.1 and shows only the diffreces of the lithotypes. These subtype description is according to the detailed core description. The color bar next to the Subtype is constant with the legend of the Detailed core description.

General observations

Organic matter in the smear slides correlate with the brownish color in the core. The organic matter often forms aggregates in the smear slides. Vivianite formed blue aggregates of up to 0.1mm size out of clay size crystals, their initially white color is changing to blue after opening. The Fe counts are anti correlating with the grain size. Al/Si anti correlate with grain size, while high ratios indicate a small grain size and vice versa.

Subtype A1

The upper most 5cm of both cores are characterized by a dark brown, organic rich, homogeneous to diffusely laminated silty clay. The organic carbon content (Corg) is around 2% to 3% of mass. The wet bulk density is on a low level around 1.1g/cm^3 to 1.3g/cm^3. The distinct dark layer shows a peak in Ba/Ti ratio, while the major elements like Al, Si, K and Ca show a down core increase together with bulk density.

Subtype A2

This diffusely laminated silt has a distinct olive tint in background color and a lowered organic carbon content of 0.66%. Several reddish patches are abundant in Subtype A2, A3 and A4. These patches are initially black and brighten after core opening.

Subtype A3

The brownish grey background color difference the Subtype A3 of Lithotype A. It has an organic carbon of 0.78%, also an increased amount in organic matter recognizable in smear slide SS12. A decrease in density falls together with a decrease of all XRF element counts and an increase in Ba/Ti ratio.

Subtype A4

A variation of greenish grey color. The brownish components disappear relative to the other

components. The organic carbon content varies from 0.5% to 0.7%. The composition is in a range of 15% to 25% of clay with and mica in the same amounts. 5% to 10% is composed of all different small diatoms and minor amounts of mafic and heavy minerals.

Subtype A5

The grey tint is less dominant as in Subtype A4. XRF counts on a small section and carbon content measurements show medium values.

Subtype A6

A local variety of Subtype A4 with distinct grey color, the greenish color disappears due to low mica content. No further data are determined of this subtype.

Subtype A7

A dark green clay interlayer with smooth changes to the A5. This special subtype has a higher mica content. The organic carbon content is on a low level at 0.58%. The content of mica is increased in comparison with Subtype A4. The Ca counts are slightly increased as well as Al and Si counts.

Subtype A8

Several of up to 10mm thick interlayers with no lamination are present in Lithotype A. The reddish color is diffusely distributed in this silty interlayers. Subtype A8 is similar to Subtype D3.

Subtype A9

Both cores contain of reddish patches or horizons which were initially black and getting brighter after opening. This horizons or patches are of the same lithology as the surrounding sediment and an additional high content of organic matter. The upper most layer is especially rich in diatoms.

Subtype A10

Diffusely laminated dark olive grey clayey silt in two short intervals in core Sils13_2 on the very bottom of core Sils13_2 at 7.7m. There reddish (initially black) patches are present. It contain no grains in sand fraction and no diatoms. The Fe/Ti ratio as well as the Al, Si, and K counts are increased in comparison to F1. The density and XRF counts of Ca and Ti are decreased.

Subtype B1

The whitish top B1 contains about 35% of clay fraction and nothing coarser than fine silt. There are centric and araphid diatoms. Al and Si increase in B1 while Ca decreases on top of B1 and increases to a mean value to the base of B1. The Fe concentration peaks at top of B1. The density increases downwards. The Al/Si ratio peaks directly on Subtype B1.

Subtype B2

B2 is a homogeneous sandy silt with lots of organic matter. There quartz, chlorite, mica and amphibole grains are together with centric, araphid, asymmetrical biraphid and surirelloid diatoms. Somme centric diatoms of the Aulacoseira class are up to 0.1mm in radial diameter, found in both cores (see Figure 14). The XRF element counts of Al and Si decreases in B2 as in B3 to a low level.

Subtype B3

The base of Lithotype B is up to fine sand in core Sils13_1 and coarse sand in Sils13_2 in grain size. The internal grading is clearly recognizable. A mean density of 2.1 g/cm^3 is in contrast with the other B subtypes. While the element counts show only weak variations.

Subtype B4

The normal graded sand with minor silt and clay of Subtype B4 is in contrast to the rest of Lithotype B not matrix supported. Subtype B4 and B5 only appears on core Sils13_2.

Subtype B5

A special clay rich layer with sand and leaf fragments only found in core Sils13_2. Similar to B3 in lithology.

Subtype C1

Subtype C1 is the least carbon rich subtype of Lithotype C with a organic carbon content of 1.5%. It forms the gradual transition of A to C with several variations in background sediment color.

Subtype C2

The dark brown background sediment with a organic carbon content of 1.9% on the upper part shows a down core decrease in density and increase in carbon content up to 3.6% in the lower part. The inorganic components are lowered. The XRF counts of Al, Si and K reaches

a minimum while Ca remains on a medium level. The Mn/Fe ratio increases in Subtype C2. The Ba/Ti ratio is increased in the lower part of this subtype. Gray clay interlayers are always higher in Al, Si, K and Ca. The Al/Si ratio is increased on each grey layer.

Subtype C3

Subtype C3 is characterized with low density values of $1.1g/cm^2$ and a dark brown color with minor variations. The Ba/Ti ratio is increased while the Mn/Fe ratio is on a low level with small increased sections.

Subtype C4

A grey clay with a increase in density and low organic carbon content forms this subtype. It shows a fluidized sediment structure. A In core Sils13_1 at 5860mm it is diffusely mixed with the dark brown component of subtype C3. It also show a decrease on the pure grey layer and a increase in the mixing area in all XRF measured elements. The Mn/Fe ratio increases on the dark sections of the mixing layer.

Subtype D1

Subtype D1 forms the transition of Lithotype C to Lithotype D. It changes from diffusely laminated to a distinct laminated sediment. Top of Subtype D1 contain more brownish tint as well as a higher organic carbon content of 0.27% in comparison to the base of D1 equal to D2 with values at 0.21%.

Subtype D2

D2 is the most common subtype of Lithotype D and has no special difference. Thinsection SDs3 in Subtype D2 contain mostly quartz and chlorite a graded layering from silt to clay fraction but no biogenic components. Additionally are heavy minerals as well as and mafic and opaque minerals are present in minor amounts (Figures 18 and 20).

Subtype D3

Subtype D3 is similar to A8, thus it is strongly affected of its major subtype and is different in stronger lamination and the more clayey matrix. The Al and Si counts are increased in contrast to the decreased Ca counts. The different ratios show no variation.

Subtype D4

The darker grey subtype has several variations in darkness due to variations in mineral content.

This is especially due to the variations in content of chlorites and amphiboles. This subtype is free of diatoms in all smear slides.

Subtype D5

This subtype has a specific yellowish background color. This color change is limited to the coarser part of the laminations. There is no clear change in mineral content on the transition of Subtype D2.

Subtype E1

This yellow variation occur on the transition of Lithotype D to Lihotype E and consist only of 5 laminas. This subtype has a high amount of clay. Greenish mica like chlorite are nearly rare in contrast to the rest of Lithotype D and E. A increase in Pb counts is located from Subtype D5 with a peak amplitude on Subtype E1. While Al, Si and K show a minor increase, Ca and Ti a minor decrease is Pb, the only element with a high amplitude excursion.

Subtype E2

A stronger grey tint differs this subtype of the other Subtypes of Lithotype E. It is abundant in the upper part of Lithotype E. Often are thin clay layers on top of a small section of this subtype. A 10cm long sample sieved to $125\mu m$ grain size, 14 grains in a size between 2mm and 8mm in maximum diameter are found. Seven grains are greenshists with chlorite, felspars and quartz. Three are serpentines, one containing a small pyrite. Mica gneisses and pure quartz grains are also present with two grains each.

Subtype E3

The strong layering with several color variation in reddish more yellowish brownish and grayish are sampled with thin section SDs 4. There are no clear changes in mineral composition recognizable. Also no clear change in grain size or organic carbon content is observed.

Subtype E4

The darker brownish subtype has a thick diffuse lamination. The carbon content is 0.15%.

Subtype F1

The darker sections in Lithotype F are of coarser grain size and more organic matter. 0.5% of organic carbon of the dark brown interlayer are in contrast to 0.2% in the olive grey background sediment. This variety has a higher content of greenish minerals like chlorite and amphiboles.

element counts of Al, Si, K are coupled to variable density. The Ba/Ti ratio is increased in the upper most part of Unit 3 and on a normal level in the rest of the core.

Subtype F2

Subtype F2 is equal to Subtype F1 except a brighter color, a lower organic carbon content and less dark interlayers. Further the density is decreased in comparison to F1.

Subtype F3

Subtype F3 is a variation in Lithotype F with a higher amount in clay and silt and less sand. Partially no sand fraction occurs. The density and the XRF element counts are in the same range as in Subtype F1.

Subtype F4

Subtype is a local variety of a homogenous dark brown olive grey muddy sand. This special color is a mixture of the dark brown interlayers with the background sediment.

Subtype F5

Subtype F5 has maximum grain size in fine sand fraction and more clay as the surrounding F1. F5 is similar to F1 in order to lithology.

A.2   Detailled core description of core Sils13_1 and Sils13_2

Legend

Subtypes

■ A1		■ B2		■ D4	
■ A2		■ B3		■ D5	
■ A3		■ B4		■ E1	
■ A4		■ B5		■ E2	
■ A5		■ C1		■ E3	
■ A6		■ C2		■ E4	
■ A7		■ C3		■ F1	
■ A8		■ C4		■ F2	
■ A9		■ D1		■ F3	
■ A10		■ D2		■ F4	
■ B1		■ D3		■ F5	
■ Event Layers					

Sediment structures

▤ Laminated	▦ Graded	
▤ Diffusely laminated	▨ Disturbed	
▤ Transition to diffusely laminated	▨ Deformed	
▢ Homogenus		

Samples

❙ XRF measurements in 1mm step size	❙ Coulomat sample
⦙ XRF measurements in 5mm step size	❙ Smear slide sample
❙ Thinsection	❙ C 14 sample

Figure 53: Legend of detailed core description of core Sils13_1 and Sils13_2

A1	Homogenious dark brown clayey silt	CG 1 1_7_sc 6.5
A9	Redish (initially black) Macrofsil rich	SS 7 1_7_sc 8.1
A1		CG 2 1_7_sc 9.5
	Transition from top brown to Type A	CG 3 1_7_sc 10.5

A2 — Diffusely laminated olive grey clayey silt with reddish(initially black) paches

Diatom free grey clay   SS 10 1_7_sc 24.5

A2 — Diffusely laminated olive grey clayey silt with reddish (initially black) paches   SS 11 1_7_sc 31.4

SS 32 1_7_sc 40.3
CG 4 1_7_sc 40.5
SS 33 1_7_sc 41
SS 34 1_7_sc 41.6
CG 5 1_7_sc 42
SS 35 1_7_sc 42
SS 36 1_7_sc 43

A3 — Diffusely laminated brownish grey clayey silt with reddish (initially black) paches

A9 — Reddish (initially black) Macrofssil rich

A3

A9 — Reddish (initially black) Macrofssil rich

A3 — Diffusely laminated brownish grey clayey silt with reddish(initially black) paches

Dark brown coarse silt to fine sand   SS 12 1_7_sc 74.4

A3 — Diffusely laminated brownish grey clayey silt with reddish (initially black) paches   C14 4 1_1_a_58.7

C14 6 1_7_sc_45.4
CG 6 1_7_sc 90

B1 — Homogenious greenish grey clay with minor fine silt, no Diatoms   CG 7 1_7_sc 92.5 / SS 8 1_7_sc 92.5

B2 — Homogenious dark brown organic rich silt   CG 8 1_7_sc 98 / SS 9 1_7_sc 100

Sils13_1_7_sc

Sils13_1_1_a

Figure 54: Detailed core description of core Sils13_1, meter 1

Homogenious dark brown organic rich silt

Diffusely laminated brownish grey clayey silt

Homogenious greenish grey clay with minor fine silt, no Diatoms

Homogenious dark brown organic rich silt

Normally graded dark brown organic rich coarse silt to sand, diffuse internal lamination

Diffusely laminated brownish grey clayey silt with reddish (initially black) paches

Reddish (initially black) Macrofsil rich

Dark brown graded silty fine sand with a whiteish top

Diffusely laminated olive grey clayey silt with reddish (initially black) paches smooth variations in brightness

CG 9 1_1_b 19

C14 6 1_1_b 24.5
CG 10 1_1_b 25.5
CG 11 1_1_b 27
CG 12 1_1_b 28.5

SS 13 1_2_b 34

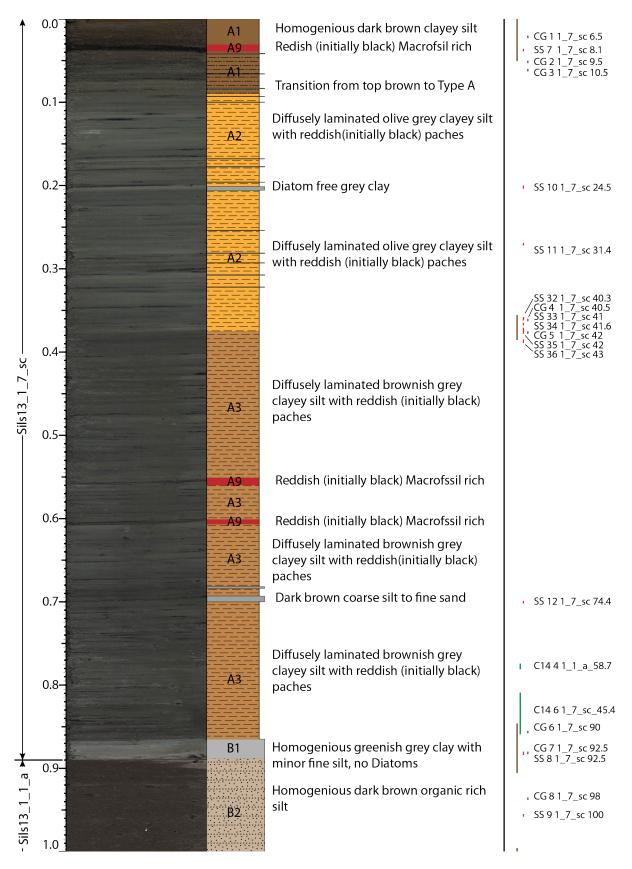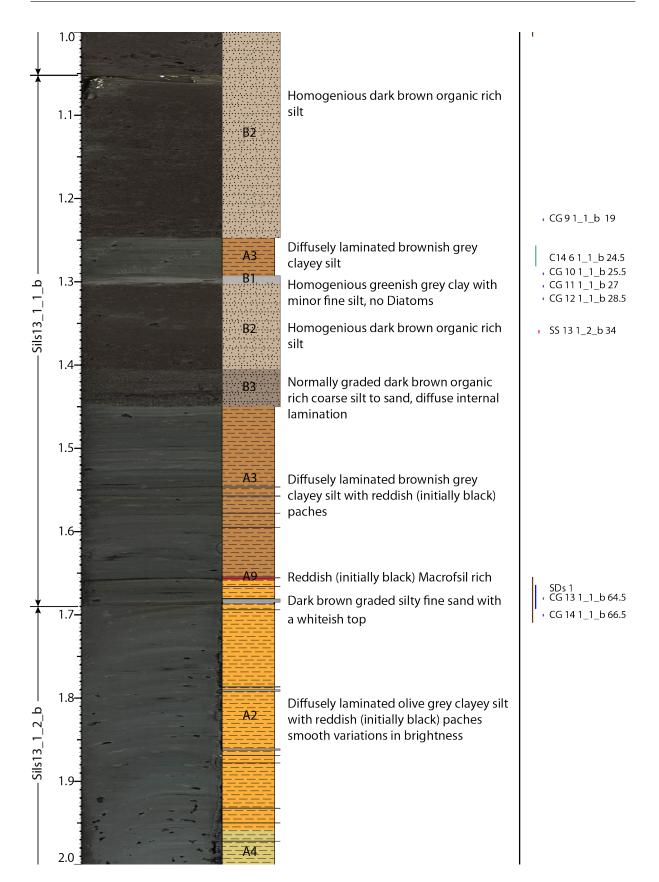SDs 1
CG 13 1_1_b 64.5
CG 14 1_1_b 66.5

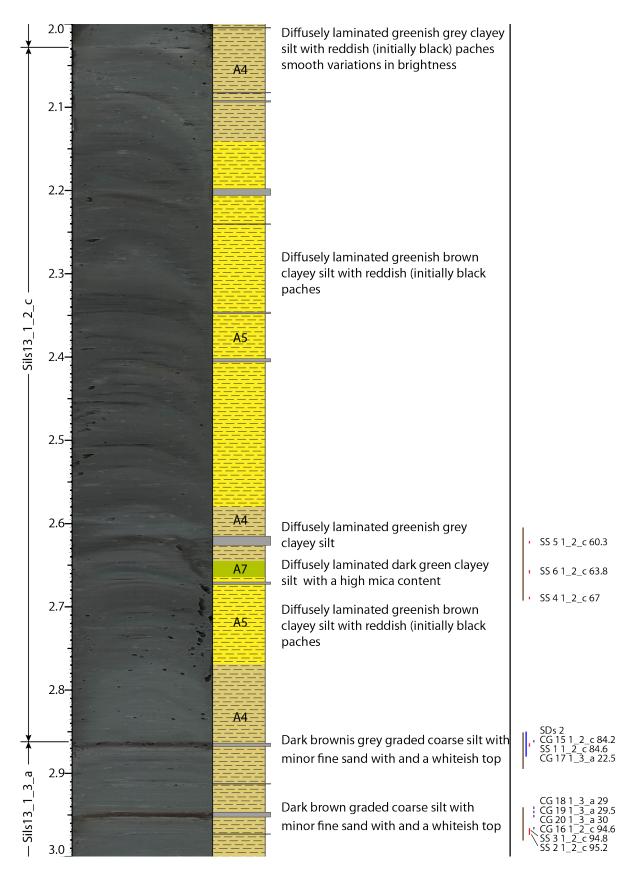**Figure 55:** Detailled core description of core Sils13_1, meter 2

Figure 56: Detailed core description of core Sils13_1, meter 3

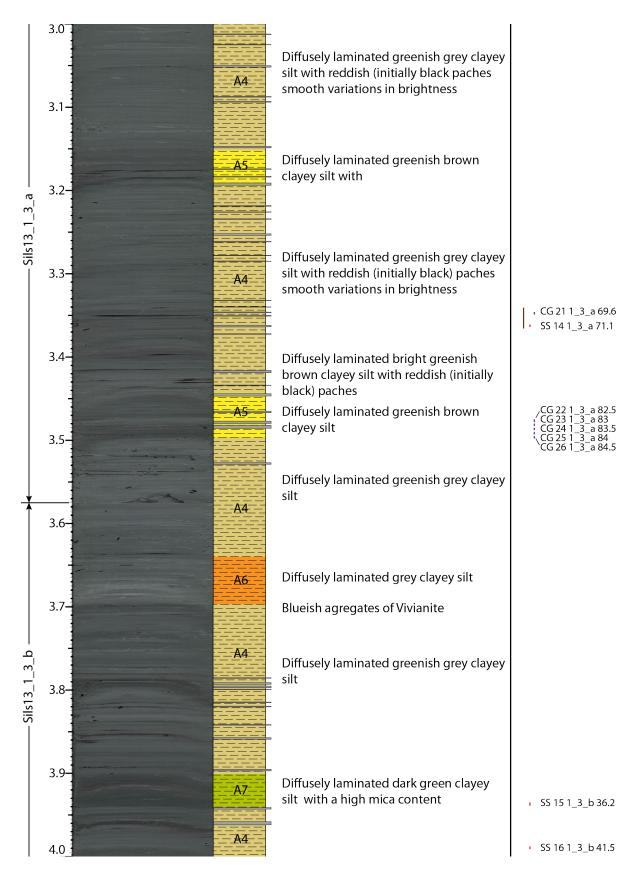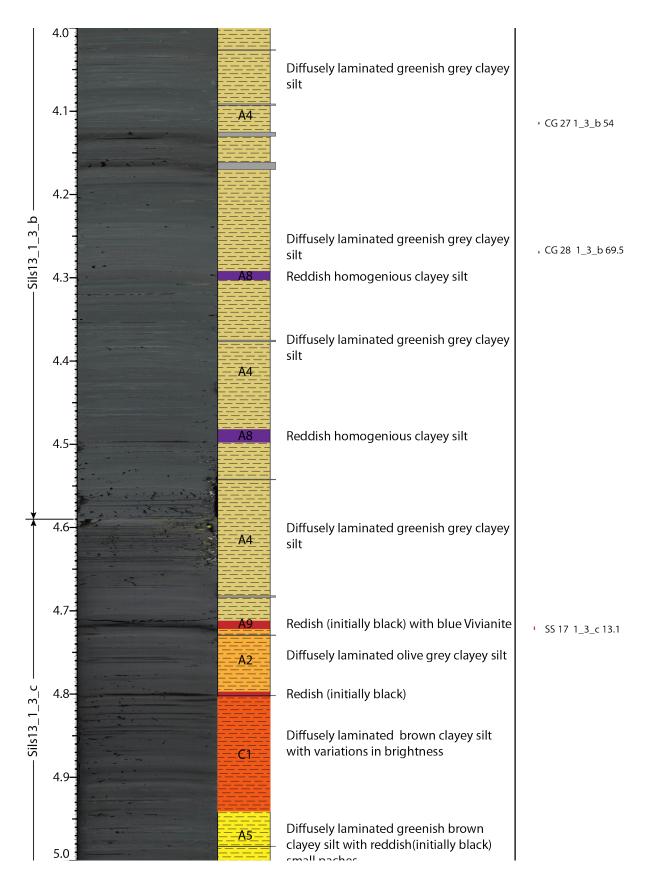**Figure 57:** Detailled core description of core Sils13_1, meter 4

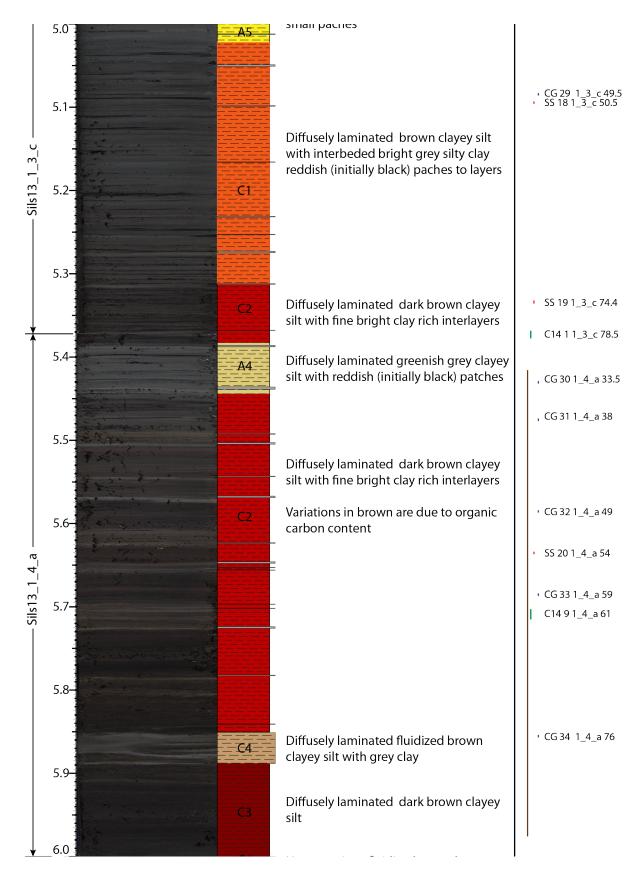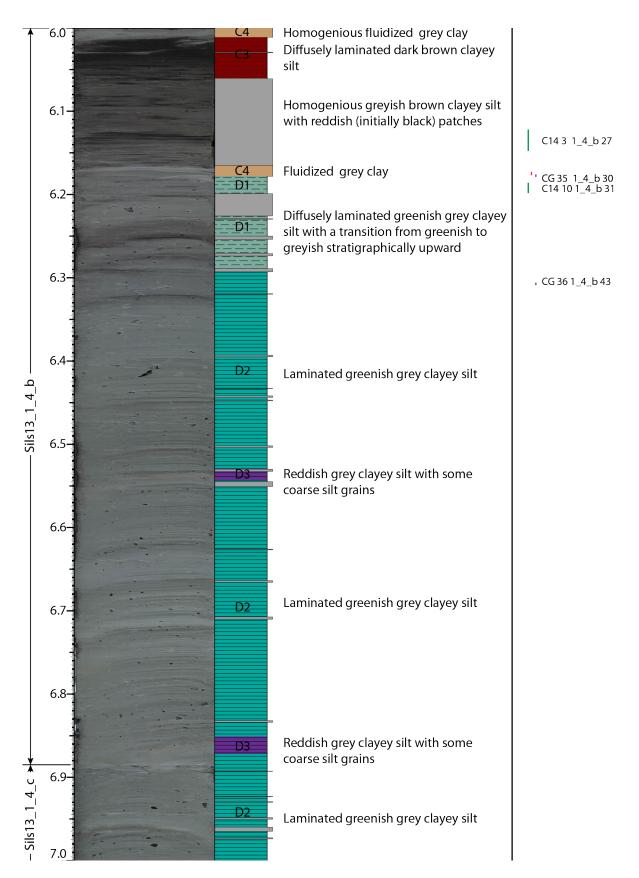**Figure 58:** Detailed core description of core Sils13_1, meter 5

small paches

A5

CG 29 1_3_c 49.5
SS 18 1_3_c 50.5

Diffusely laminated brown clayey silt
with interbeded bright grey silty clay
reddish (initially black) paches to layers

C1

C2   Diffusely laminated dark brown clayey   SS 19 1_3_c 74.4
      silt with fine bright clay rich interlayers
                                                  C14 1 1_3_c 78.5

A4   Diffusely laminated greenish grey clayey
      silt with reddish (initially black) patches

                                                  CG 30 1_4_a 33.5

                                                  CG 31 1_4_a 38

      Diffusely laminated dark brown clayey
      silt with fine bright clay rich interlayers

C2   Variations in brown are due to organic   CG 32 1_4_a 49
      carbon content

                                                  SS 20 1_4_a 54

                                                  CG 33 1_4_a 59
                                                  C14 9 1_4_a 61

C4   Diffusely laminated fluidized brown   CG 34 1_4_a 76
      clayey silt with grey clay

C3   Diffusely laminated dark brown clayey
      silt

Sils13_1_3_c

Sils13_1_4_a

Figure 59: Detailled core description of core Sils13_1, meter 6

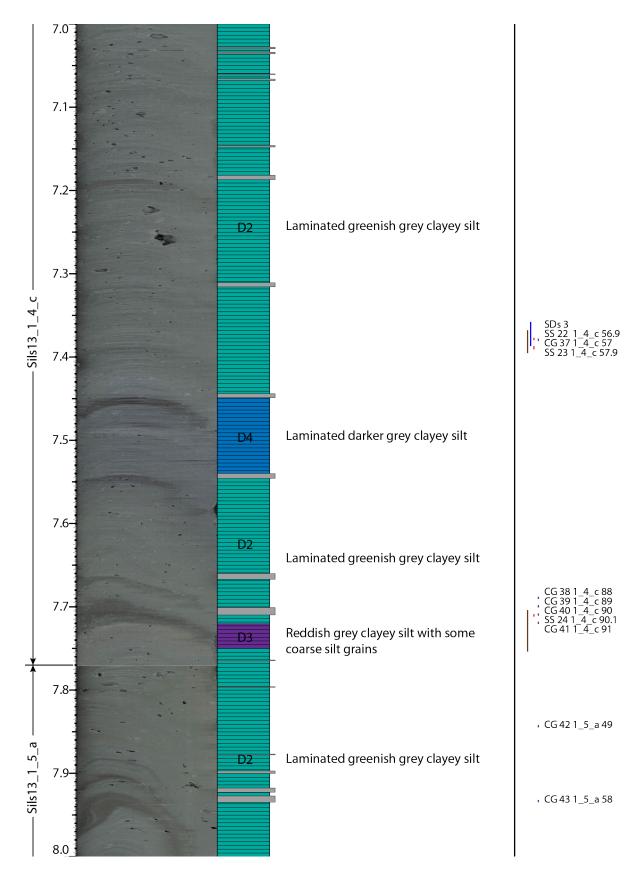**Figure 60:** Detailed core description of core Sils13_1, meter 7

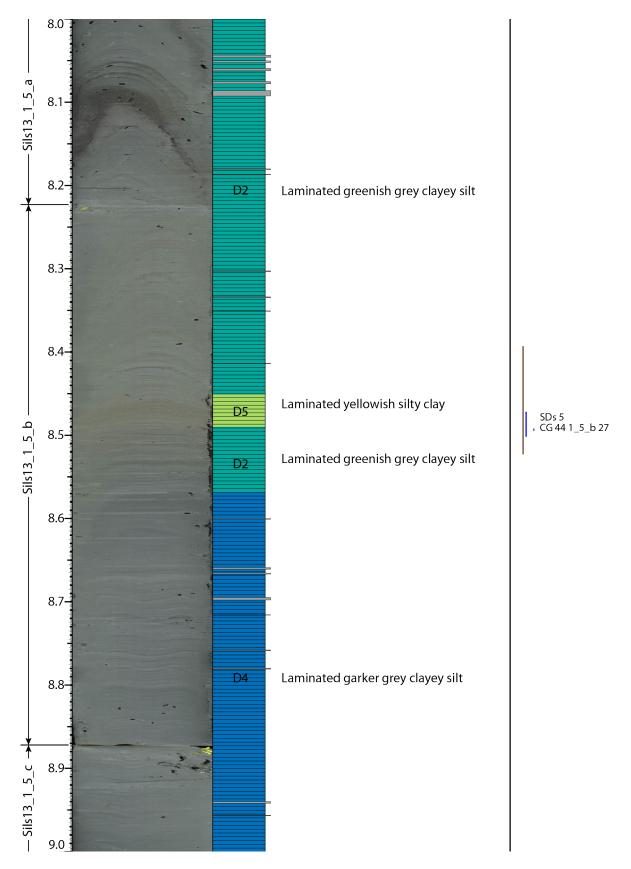**Figure 61:** Detailed core description of core Sils13_1, meter 8

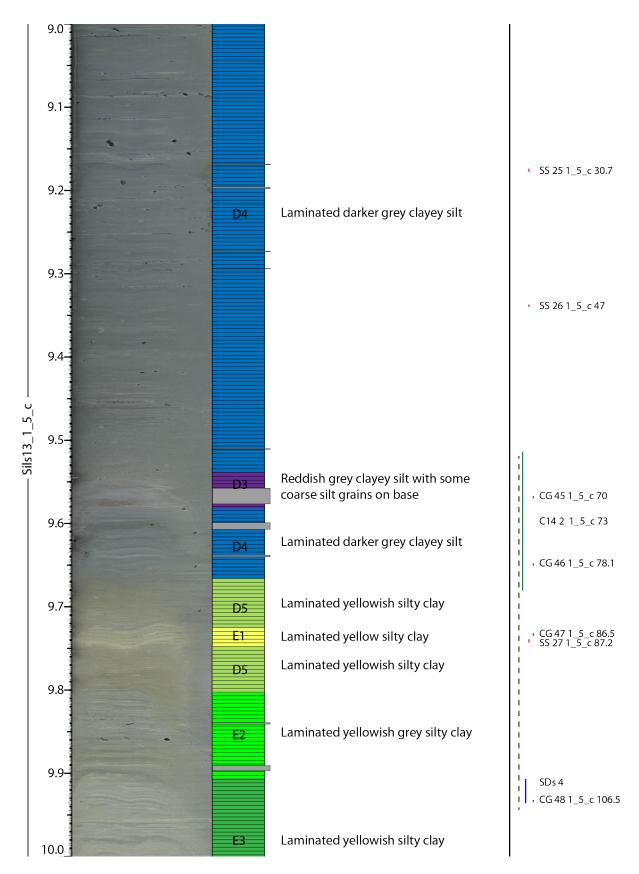**Figure 62:** Detailed core description of core Sils13_1, meter 9

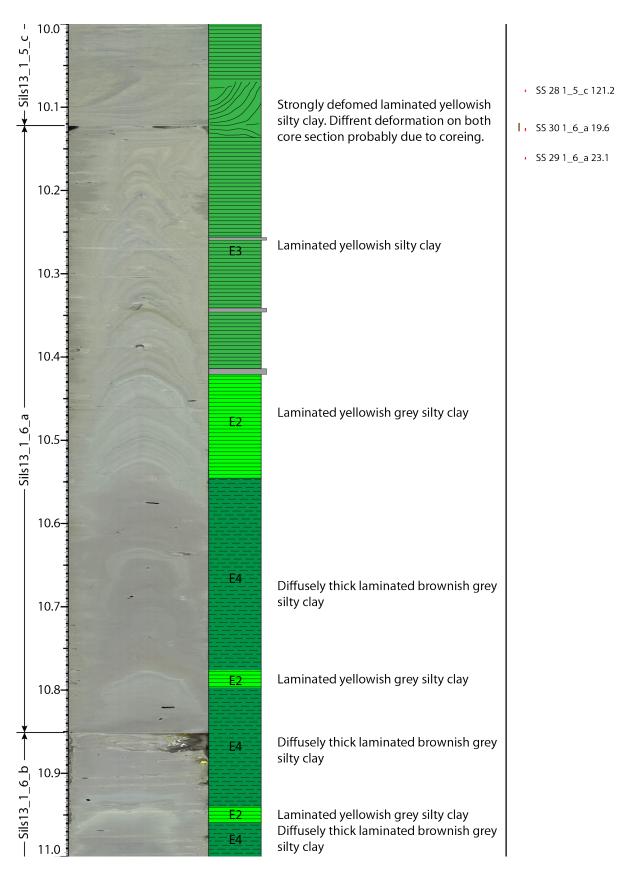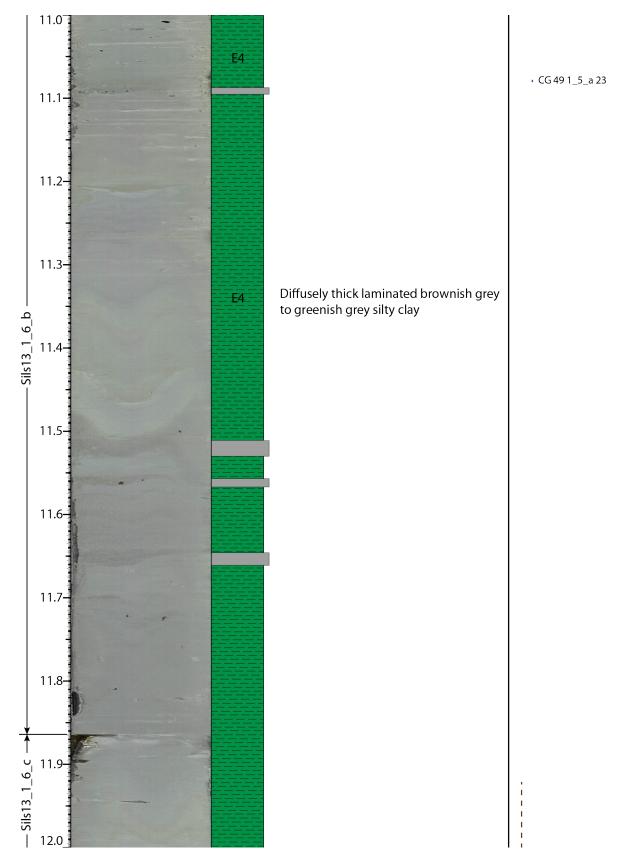**Figure 63:** Detailed core description of core Sils13_1, meter 10

Strongly defomed laminated yellowish silty clay. Diffrent deformation on both core section probably due to coreing.

SS 28 1_5_c 121.2

SS 30 1_6_a 19.6

SS 29 1_6_a 23.1

Laminated yellowish silty clay

Laminated yellowish grey silty clay

Diffusely thick laminated brownish grey silty clay

Laminated yellowish grey silty clay

Diffusely thick laminated brownish grey silty clay

Laminated yellowish grey silty clay
Diffusely thick laminated brownish grey silty clay

Figure 64: Detailed core description of core Sils13_1, meter 11

Diffusely thick laminated brownish grey to greenish grey silty clay

Figure 65: Detailed core description of core Sils13_1, meter 12
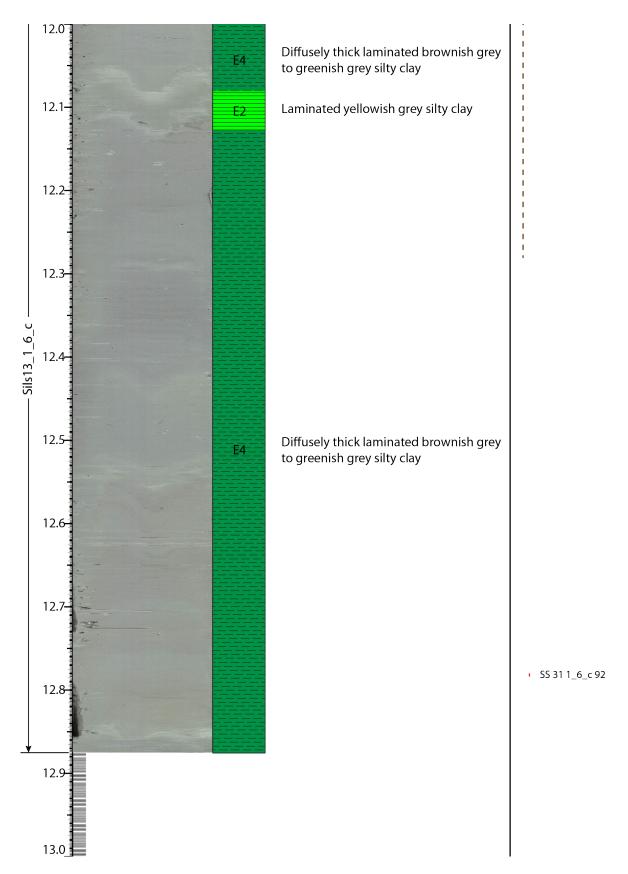
Figure 66: Detailed core description of core Sils13_1, meter 13

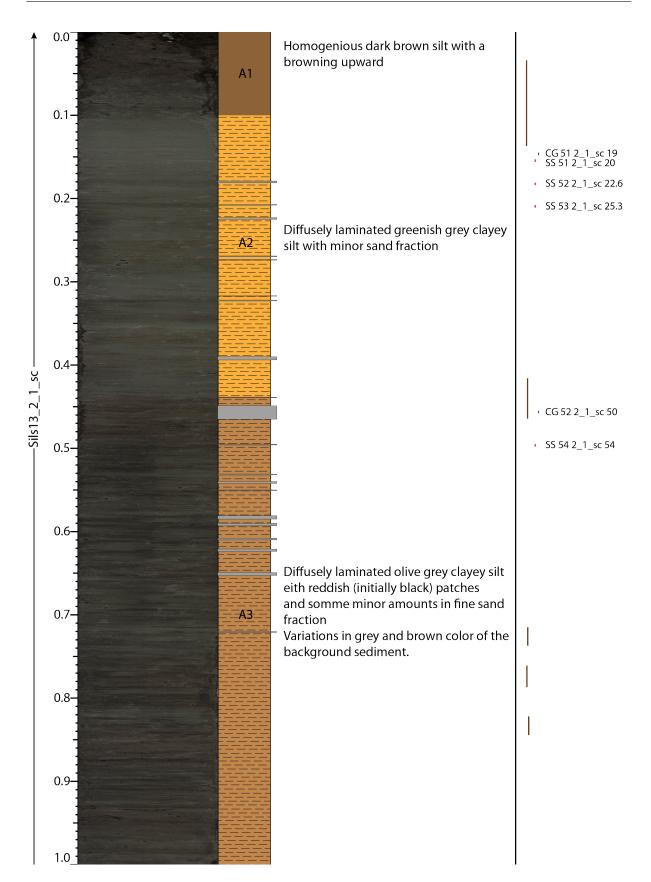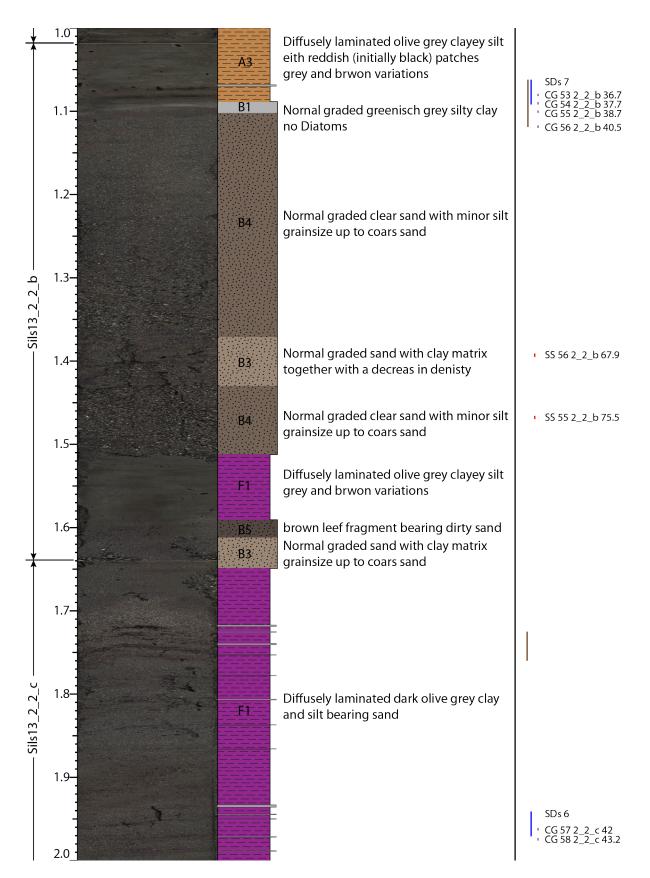**Figure 67:** Detailed core description of core Sils13_2, meter 1

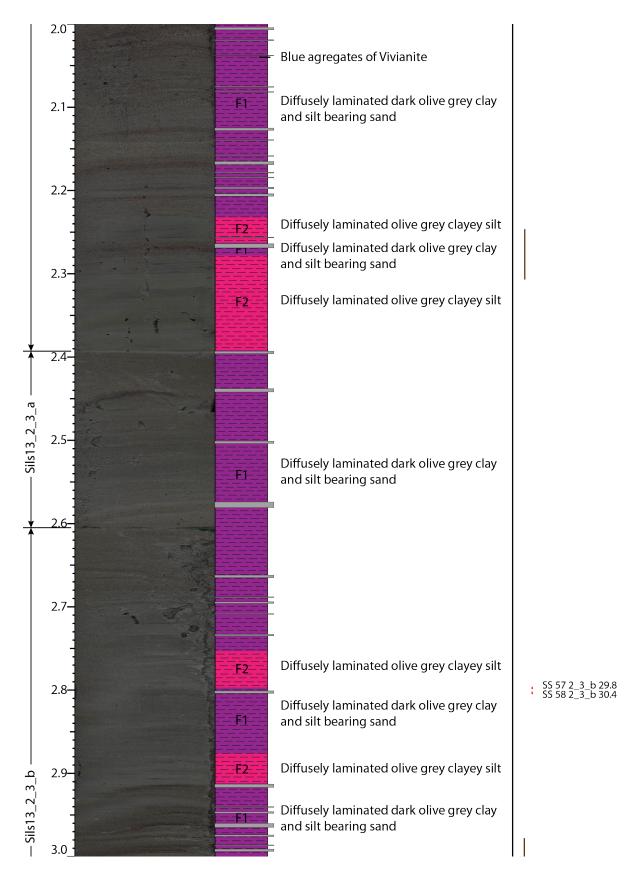Homogenious dark brown silt with a browning upward

Diffusely laminated greenish grey clayey silt with minor sand fraction

Diffusely laminated olive grey clayey silt eith reddish (initially black) patches and somme minor amounts in fine sand fraction
Variations in grey and brown color of the background sediment.

A1

A2

A3

CG 51 2_1_sc 19
SS 51 2_1_sc 20

SS 52 2_1_sc 22.6

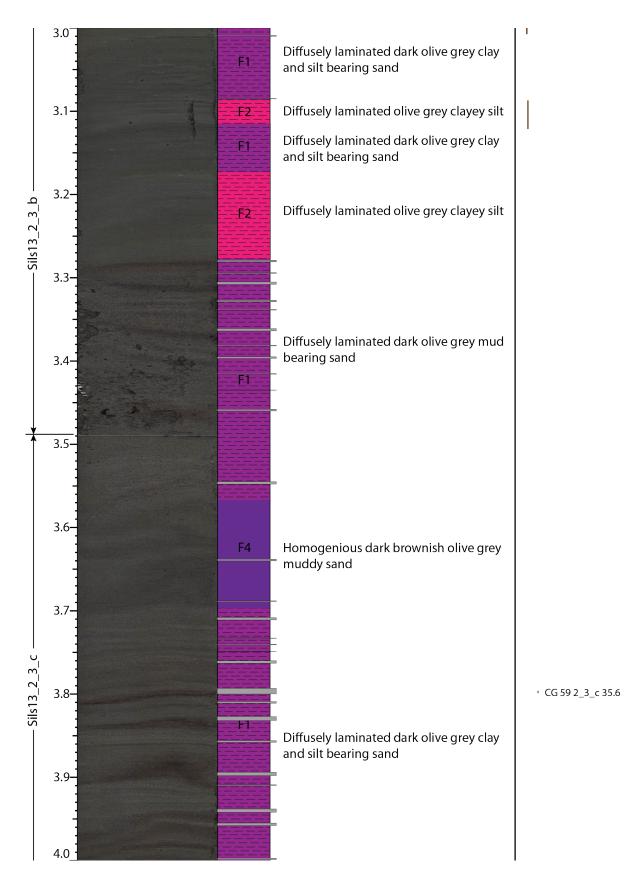SS 53 2_1_sc 25.3

CG 52 2_1_sc 50

SS 54 2_1_sc 54

Figure 68: Detailed core description of core Sils13_2, meter 2

Figure 69: Detailed core description of core Sils13_2, meter 3

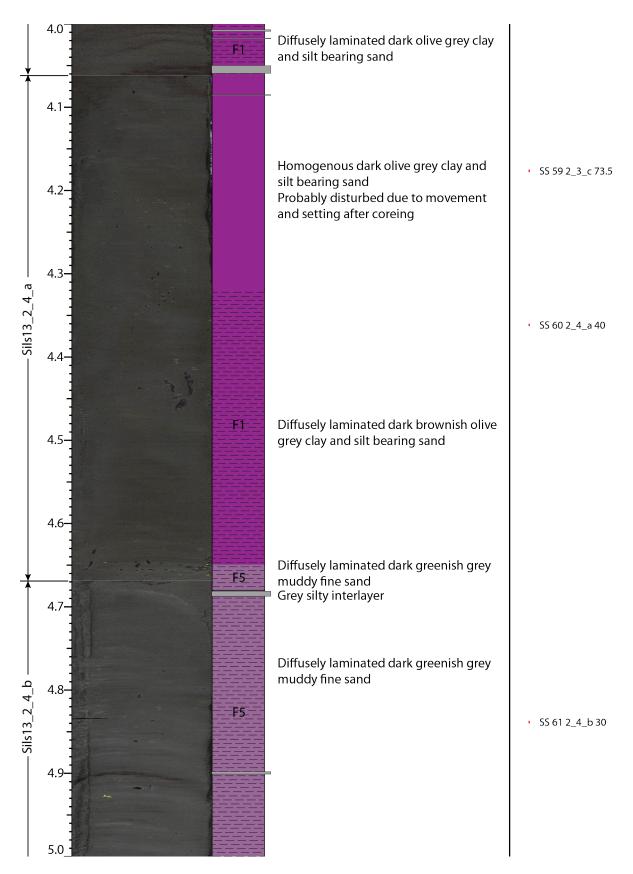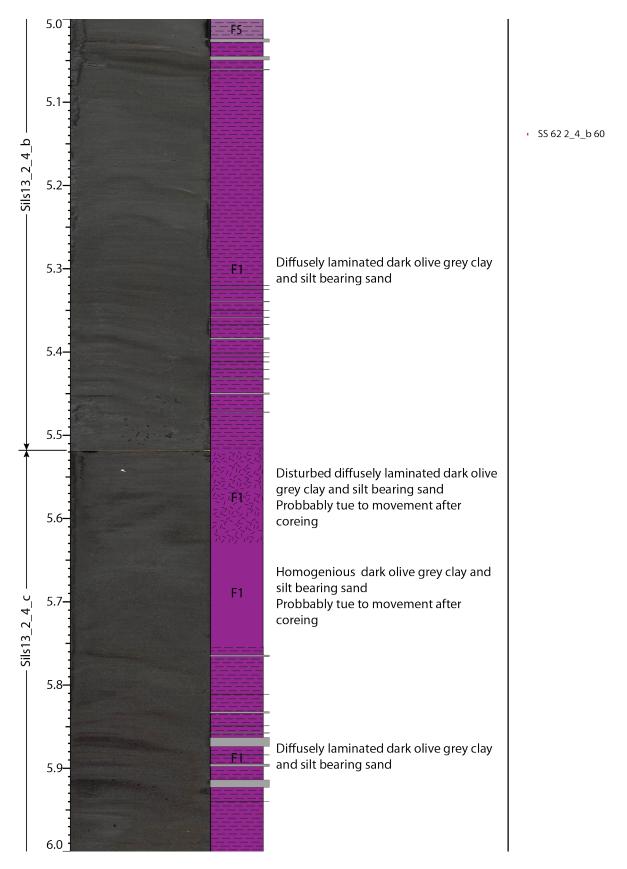**Figure 70:** Detailed core description of core Sils13_2, meter 4

Diffusely laminated dark olive grey clay and silt bearing sand

Homogenous dark olive grey clay and silt bearing sand
Probably disturbed due to movement and setting after coreing

Diffusely laminated dark brownish olive grey clay and silt bearing sand

Diffusely laminated dark greenish grey muddy fine sand
Grey silty interlayer

Diffusely laminated dark greenish grey muddy fine sand

SS 59 2_3_c 73.5

SS 60 2_4_a 40

SS 61 2_4_b 30

Figure 71: Detailed core description of core Sils13_2, meter 5

Figure 72: Detailed core description of core Sils13_2, meter 6
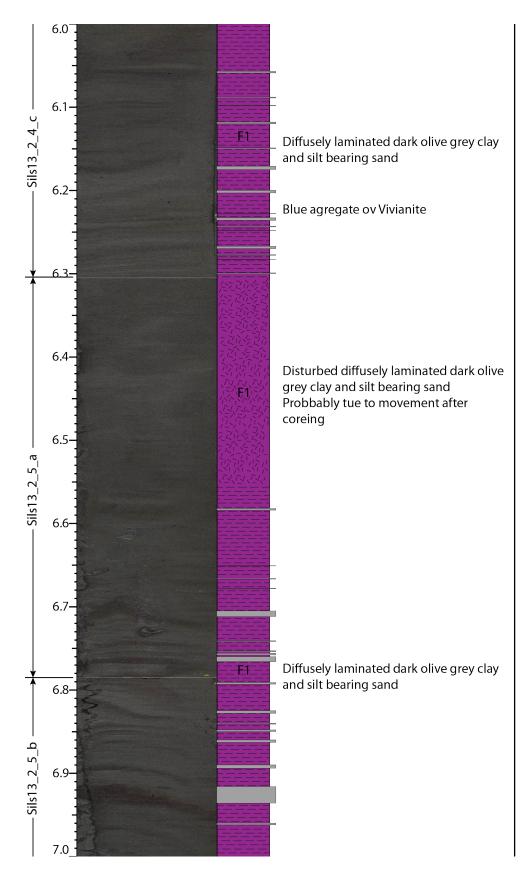
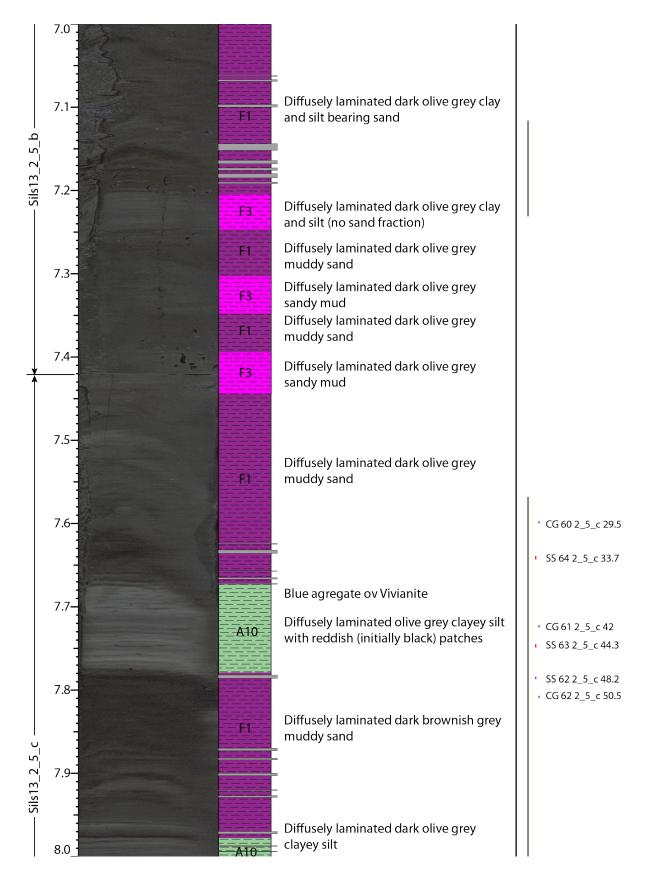**Figure 73:** Detailed core description of core Sils13_2, meter 7

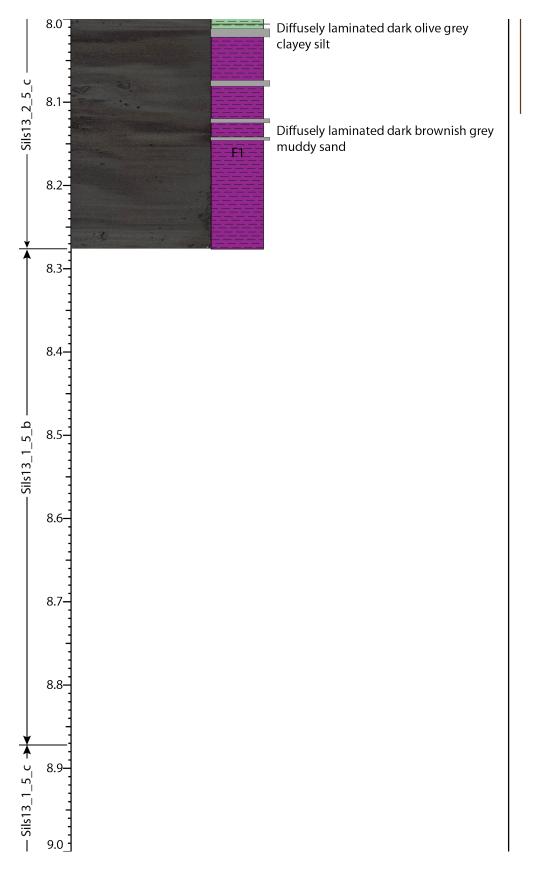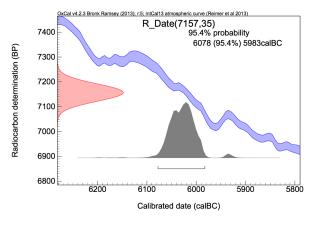**Figure 74:** Detailed core description of core Sils13_2, meter 8

Diffusely laminated dark olive grey
clayey silt

Diffusely laminated dark brownish grey
muddy sand

Figure 75: Detailed core description of core Sils13_2, meter 9

A.3   C14 calibration results of Oxcal 4.2.3
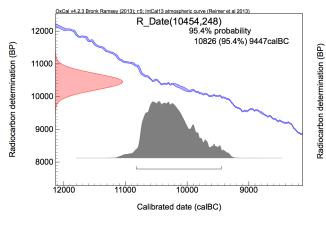
Figure 76: Oxcal results of Sample C14_1

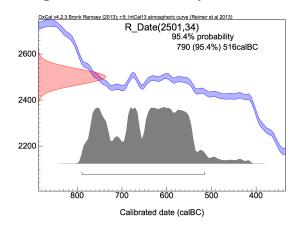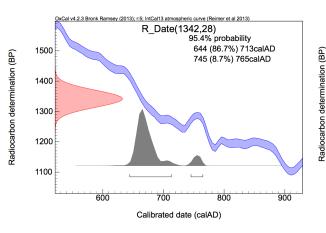**Figure 77:** Oxcal results of Sample C14_2

Figure 78: Oxcal results of Sample C14_3

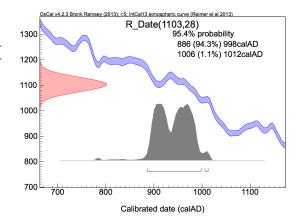**Figure 79:** Oxcal results of Sample C14_4

Figure 80: Oxcal results of Sample C14_6

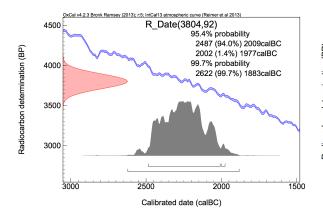**Figure 81:** Oxcal results of Sample C14_7
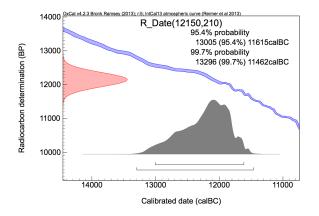
Figure 82: Oxcal results of Sample C14_8

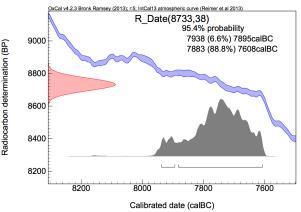**Figure 83:** Oxcal results of Sample C14_9

Figure 84: Oxcal results of Sample C14_10

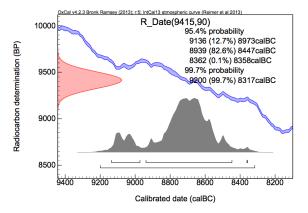**Figure 85:** Oxcal results of recalibration from the oldest sample of Leemann & Niessen (1994)

A.4   Carbon content with Coulometric method

Nr	Sample Name	Section Depth mm	Master Depth mm	Total Carbon mass %	Inorganic Carbon mass %	Organic Carbon mass %
1	Sils13_1_7_sc	6.5	20	2.865	0.006	2.859
2	Sils13_1_7_sc	9.5	50	2.161	0.127	2.034
3	Sils13_1_7_sc	10.5	60	1.543	0.000	1.543
4	Sils13_1_7_sc	40.5	360	0.663	0.000	0.663
5	Sils13_1_7_sc	42	375	0.783	0.001	0.782
6	Sils13_1_7_sc	90	855	0.827	0.003	0.824
7	Sils13_1_7_sc	92.5	880	0.374	0.000	0.374
8	Sils13_1_7_sc	98	935	3.287	0.000	3.287
9	Sils13_1_1_b	19	1224	3.343	0.000	3.343
10	Sils13_1_1_b	25.5	1289	1.048	0.000	1.048
11	Sils13_1_1_b	27	1304	0.664	0.000	0.664
12	Sils13_1_1_b	28.5	1319	3.052	0.000	3.052
13	Sils13_1_1_b	64.5	1679	1.670	0.000	1.670
14	Sils13_1_1_b	66.5	1699	0.599	0.000	0.599
15	Sils13_1_2_c	84.2	2860	0.480	0.000	0.480
16	Sils13_1_2_c	94.6	2964	1.484	0.000	1.484
17	Sils13_1_3_a	22.5	2875	0.468	0.000	0.468
18	Sils13_1_3_a	29	2940	0.614	0.000	0.614
19	Sils13_1_3_a	29.5	2945	0.997	0.000	0.997
20	Sils13_1_3_a	30	2950	1.662	0.000	1.662
21	Sils13_1_3_a	69.6	3346	0.744	0.000	0.744
22	Sils13_1_3_a	82.5	3475	0.786	0.000	0.786
23	Sils13_1_3_a	83	3480	0.585	0.000	0.585
24	Sils13_1_3_a	83.5	3485	1.073	0.000	1.073
25	Sils13_1_3_a	84	3490	1.128	0.000	1.128
26	Sils13_1_3_a	84.5	3495	0.575	0.000	0.575
27	Sils13_1_3_b	54	4113	0.864	0.000	0.864
28	Sils13_1_3_b	69.5	4268	0.634	0.000	0.634
29	Sils13_1_3_c	49.5	5083	1.56	0.000	1.560
30	Sils13_1_4_a	33.5	5429	1.032	0.000	1.032
31	Sils13_1_4_a	38	5474	1.926	0.000	1.926
32	Sils13_1_4_a	49	5584	3.600	0.000	3.60
33	Sils13_1_4_a	59	5684	3.405	0.000	3.405
34	Sils13_1_4_a	76	5854	1.387	0.000	1.387

35	Sils13_1_4_b	30	6176	0.268	0.000	0.268
36	Sils13_1_4_b	43	6306	0.210	0.000	0.21
37	Sils13_1_4_c	57	7378	0.197	0.030	0.167
38	Sils13_1_4_c	88	7688	0.317	0.146	0.171
39	Sils13_1_4_c	89	7698	0.360	0.204	0.156
40	Sils13_1_4_c	90	7708	0.366	0.202	0.164
41	Sils13_1_4_c	91	7718	0.388	0.235	0.153
42	Sils13_1_5_a	49	7842	0.403	0.228	0.175
43	Sils13_1_5_a	58	7932	0.274	0.156	0.118
44	Sils13_1_5_b	27	8492	0.177	0.000	0.177
45	SIls13_1_5_c	70	9567	0.963	0.731	0.232
46	SIls13_1_5_c	78.1	9648	0.544	0.351	0.193
47	SIls13_1_5_c	86.5	9732	0.232	0.133	0.099
48	SIls13_1_5_c	106.5	9932	0.387	0.241	0.146
49	Sils13_1_6_b	23	11078	0.841	0.69	0.151
51	Sils13_2_1_sc	19	145	0.735	0.000	0.735
52	Sils13_2_1_sc	50	455	1.676	0.000	1.676
53	Sils13_2_2_b	36.7	1079	1.559	0.006	1.553
54	Sils13_2_2_b	37.7	1089	0.888	0.001	0.887
55	Sils13_2_2_b	38.7	1099	1.182	0.000	1.182
56	Sils13_2_2_b	40.5	1117	0.356	0.153	0.203
57	Sils13_2_2_c	42	1961	0.489	0.197	0.292
58	Sils13_2_2_c	43.2	1973	0.609	0.106	0.503
59	Sils13_2_3_c	35.6	3796	0.712	0.0247	0.687
60	Sils13_2_5_c	29.5	7597	0.58	0.000	0.58
61	Sils13_2_5_c	42	7722	0.845	0.000	0.845
62	Sils13_2_5_c	50.5	7807	0.814	0.135	0.679

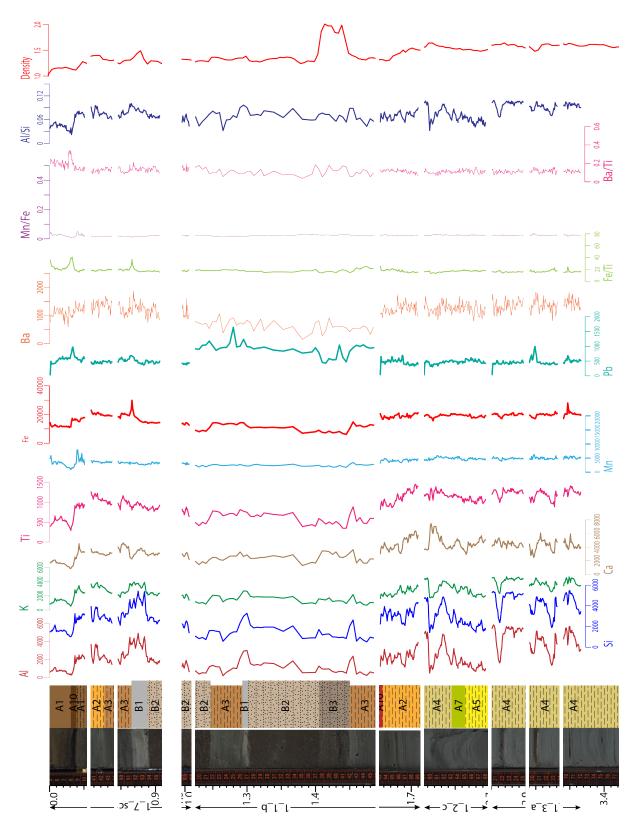## A.5 XRF Core Sils13_1
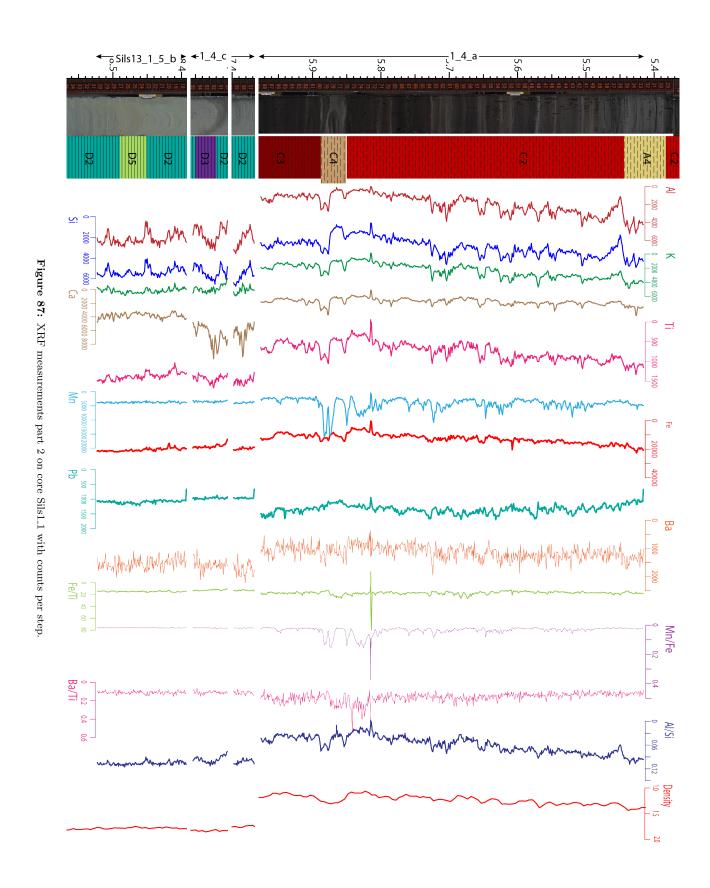
A.6 XRF Core Sils13_2

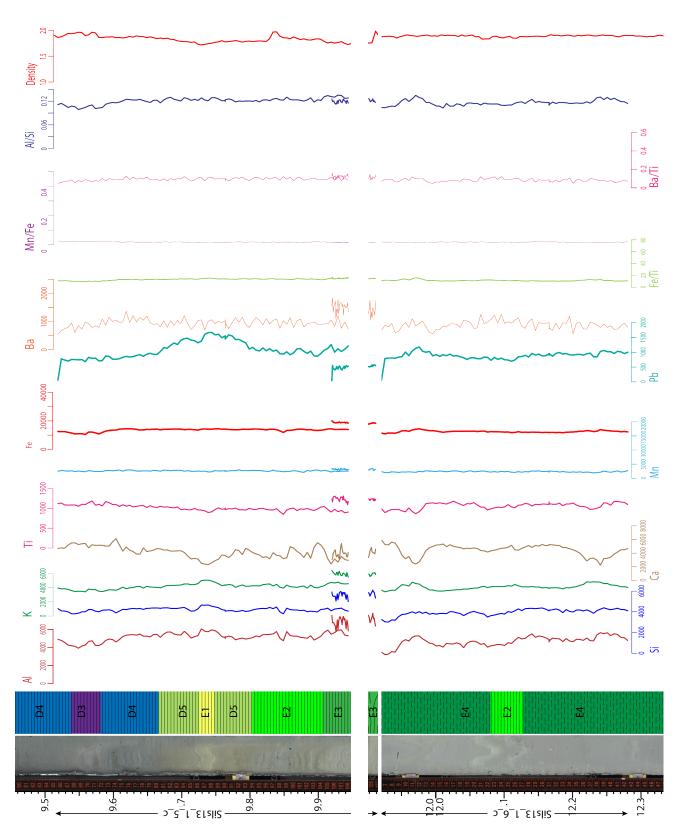**Figure 86:** XRF measurements part 1 on core Sils1_1 with counts per step.
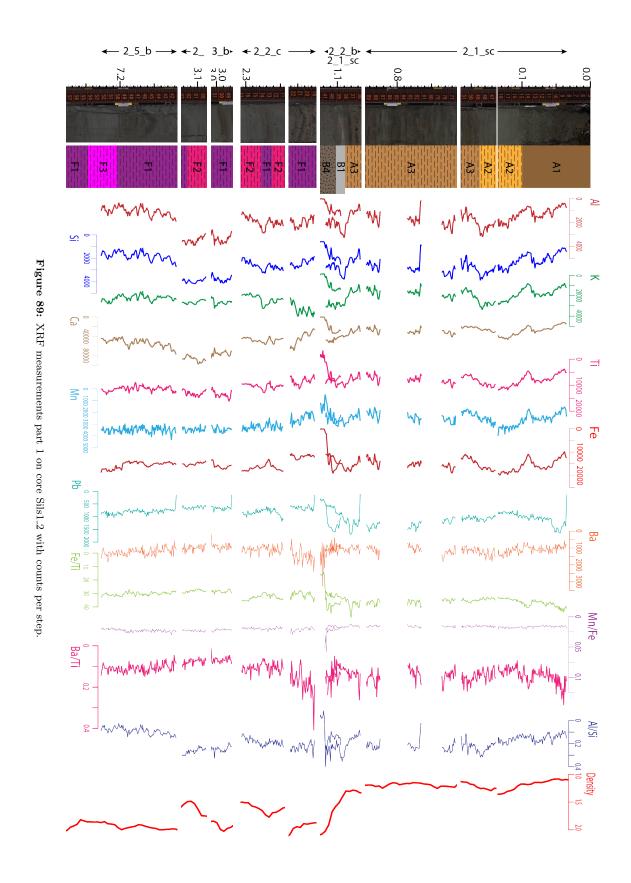
Figure 87: XRF measurements part 2 on core Sils1.1 with counts per step.
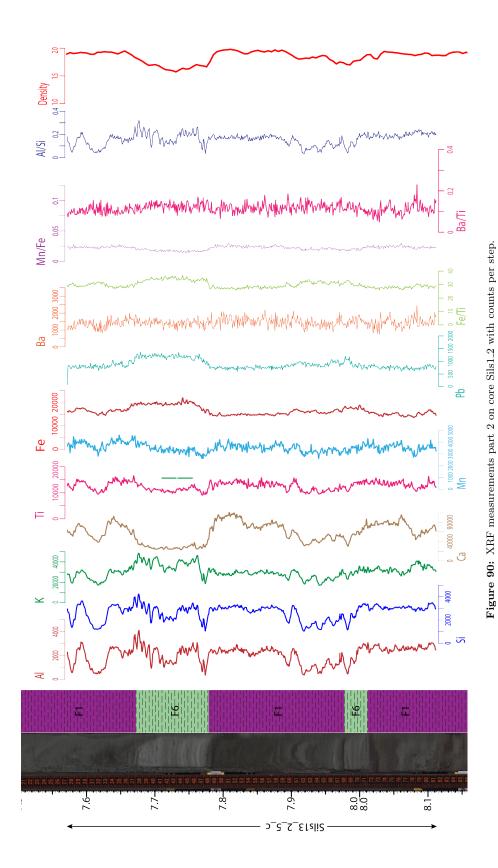
Figure 88: XRF measurements part 3 on core Sils1_1 with counts per step.

Figure 89: XRF measurements part 1 on core Sils13_2 with counts per step.

Figure 90: XRF measurements part 2 on core Sils1_2 with counts per step.

Eigenständigkeitserklärung

Die unterzeichnete Eigenständigkeitserklärung ist Bestandteil jeder während des Studiums verfassten Semester-, Bachelor- und Master-Arbeit oder anderen Abschlussarbeit (auch der jeweils elektronischen Version).

Die Dozentinnen und Dozenten können auch für andere bei ihnen verfasste schriftliche Arbeiten eine Eigenständigkeitserklärung verlangen.

_____

Ich bestätige, die vorliegende Arbeit selbständig und in eigenen Worten verfasst zu haben. Davon ausgenommen sind sprachliche und inhaltliche Korrekturvorschläge durch die Betreuer und Betreuerinnen der Arbeit.

Titel der Arbeit (in Druckschrift):

Verfasst von (in Druckschrift):
*Bei Gruppenarbeiten sind die Namen aller
Verfasserinnen und Verfasser erforderlich.*

Name(n):   **Vorname(n):**

Ich bestätige mit meiner Unterschrift:
- Ich habe keine im Merkblatt „Zitier-Knigge" beschriebene Form des Plagiats begangen.
- Ich habe alle Methoden, Daten und Arbeitsabläufe wahrheitsgetreu dokumentiert.
- Ich habe keine Daten manipuliert.
- Ich habe alle Personen erwähnt, welche die Arbeit wesentlich unterstützt haben.

Ich nehme zur Kenntnis, dass die Arbeit mit elektronischen Hilfsmitteln auf Plagiate überprüft werden kann.

Ort, Datum   **Unterschrift(en)**

*Bei Gruppenarbeiten sind die Namen aller Verfasserinnen und
Verfasser erforderlich. Durch die Unterschriften bürgen sie
gemeinsam für den gesamten Inhalt dieser schriftlichen Arbeit.*